Temperature Dependent Rate Constant for the OH + O_3 Chain Reaction via High Resolution Infrared Laser Absorption Methods

by

Bradley W. Blackmon

B. A., Hendrix College, 1995

A thesis submitted to the

Faculty of the Graduate School of the

University of Colorado in partial fulfillment

of the requirement for the degree of

Master of Science

Department of Chemistry

1998

This thesis entitled:
Temperature Dependent Rate Constant for the OH + O_3 Chain Reaction via High Resolution Infrared Laser Absorption Methods
written by Bradley W. Blackmon
has been approved for the Department of Chemistry

_____
David J. Nesbitt

_____
Veronica Vaida

Date_____

The final copy of this thesis has been examined by the signators, and we find that both the content and the form meet acceptable presentation standards of scholarly work in the above mentioned discipline.

Blackmon, Bradley Wayne (M.S., Chemistry)

Temperature Dependent Rate Constant for the OH + O_3 Chain Reaction via High Resolution Infrared Laser Absorption Methods

Theis directed by Professor David J. Nesbitt

The goal of this work is to determine the rate constant of the catalytic chain reaction of hydroxyl radical (OH) with ozone (O_3). This chain reaction proceeds in two steps: (1) $OH + O_3 \rightarrow HO_2 + O_2$, with rate constant k_1, and (2) $HO_2 + O_3 \rightarrow OH + 2\ O_2$, with rate constant k_2. These rate constants are determined by observing the temporal profile of OH radical via direct infrared absorption, and fitting the data to a model consistent with the exact solution for the entire chain reaction process. The technique of direct infrared absorption allows us to probe the kinetics over an order of magnitude greater dynamic range of ozone concentration than previous studies, which provides clearer separation between the chain induction ($k_{ind} = k_1 + k_2$), propagation, and termination steps. By utilizing a temperature-controlled flow tube, we are able to extract the temperature dependence of the kinetics as well. The Arrhenius form for $k_{ind} = k_1 + k_2$ between 334 and 240K is determined to be $k_{ind}(T)\ \left[\frac{\text{cm}^3}{\text{sec}}\right] = \left(2.93^{+0.42}_{-0.38}\right) \times 10^{-12}\ \ \exp\left(\frac{-(1030 \pm 50)\text{K}}{T(\text{K})}\right)$. This value is significantly higher than the values currently recommended for use in atmospheric models. Kinetic analysis of k_{ind} below 240K and the ratio of k_2/k_{ind} have also been investigated.

To All My Teachers in Life

ACKNOWLEDGEMENTS

There are many people who have made this thesis, and this work, possible. First, and foremost, I would like to thank my wife, Ida, for giving me the strength and courage to look within myself and find that which truly makes me happy. Thank you for your encouragement and support during this very hectic time. She has made me realize what is really important, and has shown me the magic inherent in life.

I would also like to thank the very many people with whom I have had the honor of working. Thanks to Bill Chapman, for his support and encouragement, both in the lab and out. I would also like to thank Sergey Nizkorodov, for all his hard work fitting the mountains of data; Scott Davis, for all the lunch-time conversations; and Tyson Nunemacher, for showing me how to brew the best pale ale I've ever tasted. Thank you to everyone else who made my stay here much more bearable: Ondrej Votava, Joanna Fair, David "Charlie" Anderson, Dairene Uy, Nikki Delaney, Tanya Meyers, Stuart Macenzie, Joe Kim, Hendrik Hamann, and Barb Tennis, I would also like to thank my parents and brother: Gary, Kathy, and Ryan, for their constant love and support.

Finally, I would like to thank my advisor, David Nesbitt, for teaching me to be a truth seeker, and whose dedication and determination will always keep me in awe.

CONTENTS

CHAPTER

TABLES

Table

FIGURES

Figure

CHAPTER 1

INTRODUCTION

With the discovery of the ozone hole over Antarctica, the catalytic destruction of ozone has become the subject of much research and debate. Why are these catalytic destruction cycles so important to the chemistry of the stratosphere? In order to answer this question, we must look back in history.

As far back as 1881, scientists have been aware of the existence of the ozone layer[1]. The ozone layer is a region of the stratosphere with an unusually high number density of ozone (O_3). Chapman, in an attempt to explain the chemical processes that form the ozone layer, proposed the following cycle[2]:

$$O_2 + h\nu \rightarrow O + O \quad (1.1)$$

$$O + O_2 + M \rightarrow O_3 + M \quad (1.2)$$

$$O_3 + h\nu \rightarrow O + O_2 \quad (1.3)$$

$$O + O_3 \rightarrow 2\ O_2 \quad (1.4)$$

$$O + O + M \rightarrow O_2 + M \quad (1.5)$$

However, subsequent laboratory measurements proved reaction (1.4) to be much too slow to destroy ozone at the rate it is produced globally. There had to be another pathway through which to destroy ozone and account for the observed stratospheric ozone concentrations (shown in figure 1-1). These other, more efficient pathways consists of *catalytic* chain reactions. A simple catalytic ozone loss process is shown below:

$$X + O_3 \rightarrow XO + O_2 \qquad (1.6)$$

$$XO + O \rightarrow X + O_2 \qquad (1.7)$$

$$\overline{O + O_3 \rightarrow O_2 + O_2} \qquad (1.8)$$

where X = H and OH (HO_x), NO (NO_x), and Cl (ClO_x).

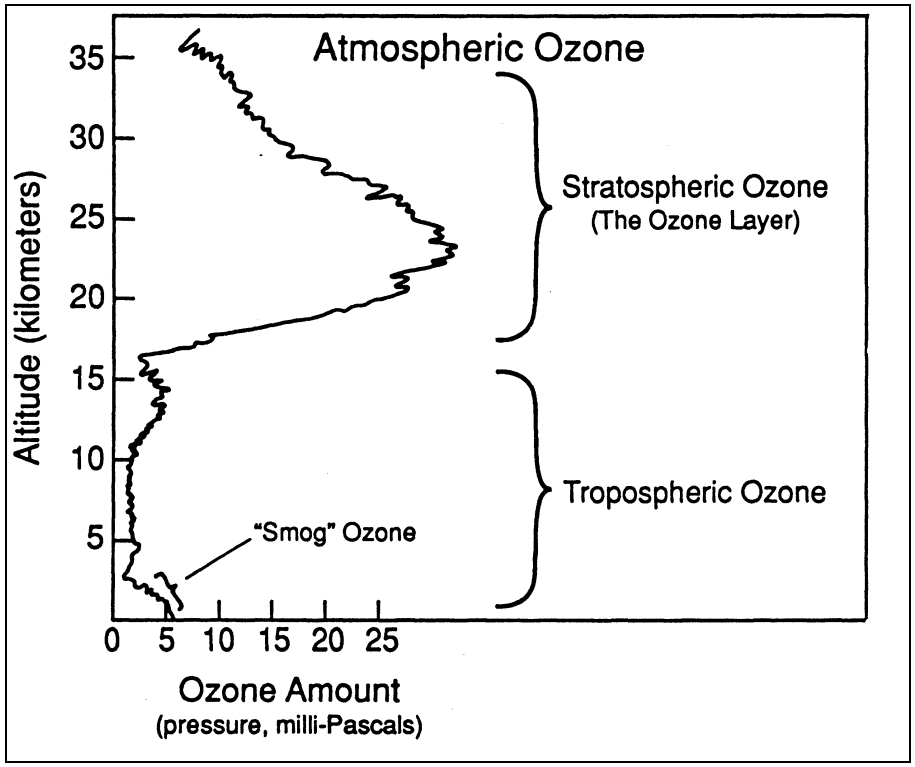

Figure 1-1. Ozone density as a function of altitude.

It is important to notice that the catalytic species denoted by X is not consumed in the reaction. This allows trace atmospheric species to have non-negligible effects on other, more abundant species in the atmosphere.

There are many chain reactions, involving hydrogen, nitrogen, and chlorine radicals that lead to the net destruction of ozone.[3] However, the catalytic chain reaction involving OH radical is important for many reasons.

$$OH + O_3 \rightarrow HO_2 + O_2 \qquad k_1 \qquad (1.9)$$

$$HO_2 + O_3 \rightarrow OH + 2\,O_2 \qquad k_2 \qquad (1.10)$$

Although not affiliated with the mechanism for the Antarctic ozone hole, the above catalytic reaction is responsible for roughly *half* of the global ozone loss.[4] This cycle is active in the mid-latitudes, at an altitude of ≤ 25 km, which is in the lower stratosphere, just above the tropopause (see figure 1-2). Unlike the other chain reactions involving ozone, the above cycle does not involve O atoms as a reactant. This is important because, in the lower stratosphere, three-body recombination of O atoms with O_2 is quite rapid. Therefore, O atom concentrations are quite low in this region.

Stratospheric OH is created through two primary pathways. The most direct pathway is through the reaction of stratospheric H_2O with $O(^1D)$.

$$O_3 + h\nu \rightarrow O_2 + O(^1D) \qquad (1.11)$$

$$H_2O + O(^1D) \rightarrow 2\,OH \qquad (1.12)$$

$$CH_4 + O(^1D) \rightarrow OH + CH_3 \qquad (1.13)$$

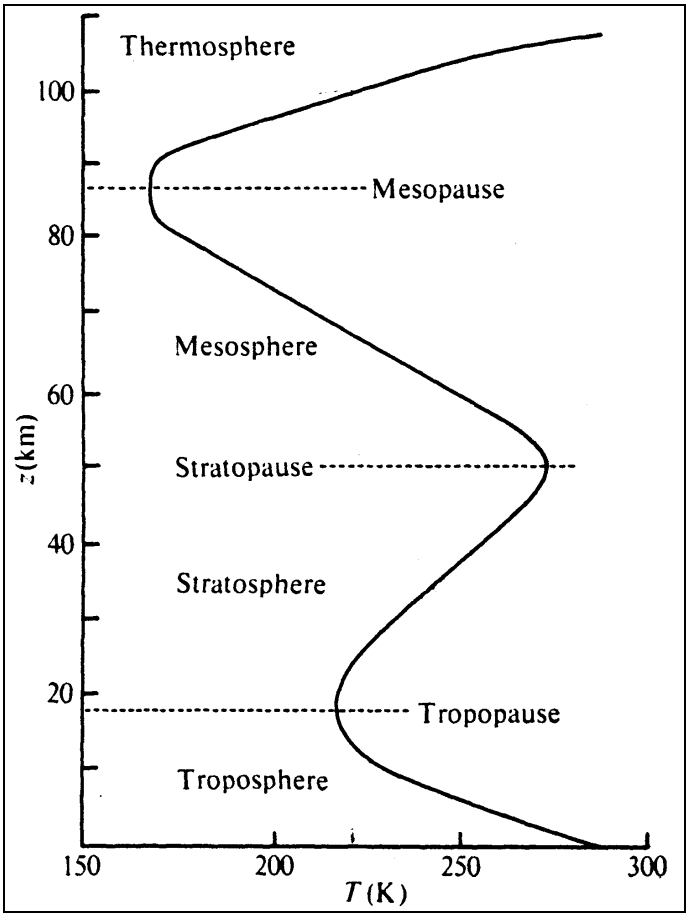

Figure 1-2. Temperature as a function of altitude. Also shown is the divisions of the various layers of the atmosphere.

However, the stratosphere is known to be very dry. This is due primarily to the tropopause, which acts as a "cold-trap" preventing the exchange of H_2O from the troposphere (see figure 1-2). Therefore, reaction (1.13) acts as the primary source for stratospheric OH.

Stratospheric, supersonic aircraft threaten to disturb the natural abundances of CH_4 and H_2O. These aircraft operate in the region of the stratosphere where the OH/O_3 chain reaction has the most effect. Therefore, it is important to discover

what damage, if any, the increased HO_x and NO_x levels will have on global ozone concentrations.

Previous measurements of the OH + O_3 reaction (1.9) can be found in the literature.[5-8] The most recent measurement has been performed by Ravishankara et al. [6] using a flash photolyisis – resonance fluorescence system over a temperature range of 238 – 257 K. In their experiment, Ravishankara et al. used LIF detection to monitor the temporal profile of OH radical in a temperature-controlled flow cell. Ravishankara et al. only report a rate constant for reaction (1.9), which is roughly 30 times faster[6,9] than reaction (1.10). Because of their dependence on H_2O as both a precursor and vibrational relaxer, Ravishankara et al. could not extend their measurements below 240 K. Other measurements have been made as well. However, all the measurements have used a resonance fluorescence system to measure the concentration of OH radical.

These resonance fluorescence systems detect OH by observing fluorescence from the first excited electronic state[10] of OH, which is populated via an initial "pump" flash of UV light. The resulting fluorescence[11,12] occurs at approximately 309 nm. Unfortunately, ozone has a non-negligible absorption cross section at these wavelengths[13]. Therefore, as ozone number density increases, the absorption will also increase, resulting in an overall decrease in observed OH signal. In addition, the photolysis of ozone by the initial pump beam added to the photolysis of ozone from the subsequent fluorescence will increase the total radical population density, which can cause complications in the kinetics, especially at low temperatures. In order to counter these adverse effects, it is necessary to limit the total

amount of ozone present in the system. In previous experiments, the highest reported ozone density[5-8] is 7 x 10^{15} molecules/cm^3. By using a completely different method for detecting OH radicals, i.e. direct infrared absorption, we are free of this ozone density limitation.

Measurements of the $HO_2 + O_3$ reaction (1.10) can be found in the literature as well.[9,14,15] Sinha et al. report a directly-measured value for k_2 based on the first order decay of isotopically labeled $H^{18}O_2$ in excess $^{16}O_3$ via laser magnetic resonance (LMR) detection.[9] Other, less direct, measurements of k_2 by Zahniser et al.[14] and Manzanares et al.[15] involved use of a scavenger (C_2F_3Cl) that preferentially reacts with OH over HO_2, thereby removing OH radicals from the chain. By utilizing isotopic substitution, Sinha et al. were able to avoid using an OH scavenger, which interferes[9] with the kinetics at temperatures above 360K. Their measurements span a temperature range of 243 – 413K, and show upward curvature in the Arrhenius plot at low temperatures, thus making extrapolation to lower temperatures more difficult and prone to error. We propose using a completely different method for measuring k_2 based on the full chain reaction kinetics of the OH/O_3 system.

The purpose of this work is threefold: (1) to measure k_1 over a broader range of ozone concentrations, (2) to extend the measurement of k_1 to lower temperatures, and (3) to measure k_1 and k_2 simultaneously. This work uses direct infrared absorption to monitor the OH radical concentration. Therefore, we are able to vary the ozone concentration over a range an order of magnitude greater than that of previous measurements. The OH decay is due primarily to reaction (1.9).

However, the resulting increase in signal at these greater ozone concentrations allows us to analyze information contained in the tail of the OH decay, yielding information on the slower reaction (1.10) (see Chapter 3 for a more detailed description of the kinetic analysis of the OH/O_3 chain reaction).

Although the primary thrust of this thesis is the kinetics of the OH/O_3 chain reaction, our laboratory has been exploring other interesting areas of chemical dynamics. One such experiment is the determination of the vibrational/rotational nascent state distribution of the HF(v,J) products from the reaction of F atom with H_2 via direct infrared absorption. For this reason, this thesis includes a chapter outlining some of our findings.

This thesis is outlined as follows. Chapter 2 contains the experimental details of the determination of the rate constant for the OH/O_3 chain reaction. Chapter 3 presents data and results from this study, including the initial room-temperature determination, systematic checks, and the temperature dependance. Finally, chapter 4 contains data and results pertaining to the nascent state distribution of HF(v,J) resulting from the reaction of $F + H_2$. Also included in this thesis is instructions and code necessary to operate the DSP transient digitizer used in these experiments.

References for Chapter 1

1 W. N. Hartley, *J. Chem. Soc.* **39,** 111 (1881).

2 S. A. Chapman, *Mem. Roy. Meterol. Soc.* **3,** 103 (1930).

3 R. P. Wayne, *Chemistry of Atmospheres* (Clarendon Press, Oxford, 1991).

4 *Scientific Assessment of Ozone Depletion: 1994*, Vol. , edited by C. A. Ennis (World Meterological Organization, 1995).

5 J. G. Anderson and F. Kaufman, *Chem. Phys. Lett.* **19,** 483 (1973).

6 A. R. Ravishankara, P. H. Wine, and A. O. Langford, *J. Chem. Phys.* **15,** 984 (1978).

7 C. A. Smith, L. T. Molina, J. J. Lamb, and M. J. Molina, *Int. J. Chem. Kin.* **16,** 42 (1984).

8 M. J. Kurylo, *Chem. Phys. Lett.* **23,** 467 (1973).

9 A. Sinha, E. R. Lovejoy, and C. J. Howard, *J. Chem. Phys.* **87,** 2122 (1987).

10 R. A. Sutherland and R. A. Anderson, *J. Chem. Phys.* **58,** 1226 (1973).

11 J. A. Coxon, A. D. Sapey, and R. A. Copeland, *J. Mol. Spec.* **145,** 41 (1991).

12 G. H. Dieke and H. M. Crosswhite, *J. Quant. Spectrosc. Radiat. Transfer* **2,** 97 (1962).

13 J. Brion, A. Chakir, D. Daumont, J. Malicet, and C. Parisse, *Chem. Phys. Lett.* **213,** 610 (1993).

14 M. S. Zahniser and C. J. Howard, *J. Chem. Phys.* **73,** 1620 (1980).

15 E. R. Manzanares, M. Suto, and L. C. Lee, *J. Chem. Phys.* **85,** 5027 (1986).

CHAPTER 2

EXPERIMENTAL

2.1 Introduction

This experiment uses a temperature-controlled flash kinetic spectrometer to measure the rate of the following chain reaction:

$$OH + O_3 \rightarrow HO_2 + O_2 \qquad (k_1) \qquad (2.1)$$

$$HO_2 + O_3 \rightarrow OH + 2\ O_2. \qquad (k_2) \qquad (2.2)$$

The rate constant is measured by monitoring the time-dependant OH radical concentration via direct infrared absorption. The infrared source is an F-center laser, tuned to the $v=1 \leftarrow 0$ $P(5/2)1^-$ transition of OH radical, which probes the most populated state at room temperature. The P branch is chosen over the R branch because the Einstein A coefficient is slightly larger[1]. In order to simplify the kinetics, $[O_3]$ is at least 1000 times greater than [OH], which results in pseudo-first order behavior.

2.2 The Experimental Apparatus

The apparatus used in this experiment is the temperature-controlled flash kinetic spectrometer shown in figure 2-1.[2,3] The spectrometer consists of a temperature-controlled flow tube into which various precursor and reactive gases are introduced.

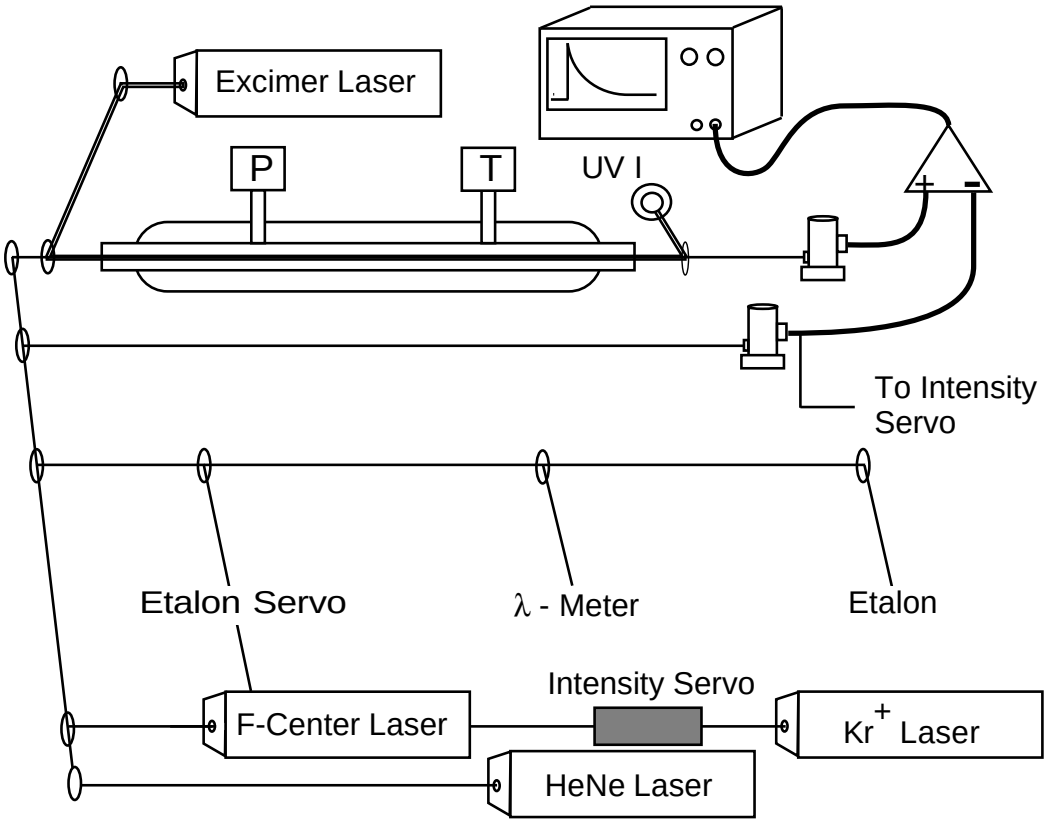

Figure 2-1. Experimental setup. $O(^1D)$ is created by photolysis of O_3 at 308 nm. The $O(^1D)$ reacts quickly with H_2O and H_2 to from OH. The time-dependant OH concentration is then probed by the F-center laser tuned to the $v=1 \leftarrow 0$ $P(5/2)1^-$ transition. The infrared light is detected by liquid-nitrogen cooled InSb detectors. Signal subtraction and the intensity servo serve to reduce common-mode noise.

The reaction scheme, shown in figure 2-2, is initiated by a 10 ns pulse from a XeCl excimer laser (308 nm). The UV light serves to photolyze 1% of the ozone

present in the excimer beam, based on a beam diameter of 1 cm, a pulse energy of 0.5 mJ/pulse, and a 308 nm ozone cross section of 1.35×10^{-19} cm^2. At room temperature[4], the branching ratio for the $O(^1D)$ product from the ozone photolysis is 80%. Following the photolysis, the $O(^1D)$ is free to react with precursor gases (H_2 and H_2O).

$O(^1D) + H_2O \rightarrow OH + OH$ ($k_3 = 2.2 \times 10^{-10}$ cm^3/sec) (2.3)

$O(^1D) + H_2 \rightarrow OH + H$ ($k_4 = 1.0 \times 10^{-10} cm^3$/sec) (2.4)

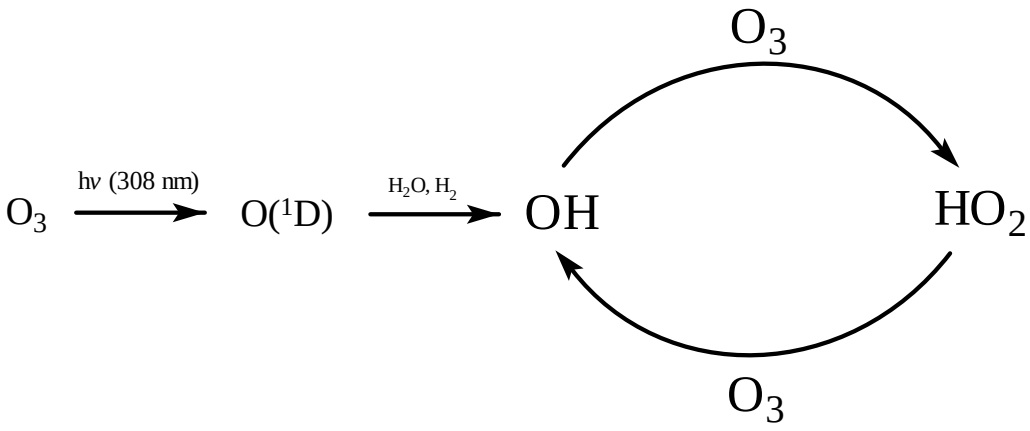

Figure 2-2. Reaction scheme of the $OH/HO_2/O_3$ chain reaction. An excimer laser tuned to 308 nm photolyzes approximately 1% of the ozone in the 1cm diameter excimer beam. The resulting $O(^1D)$ then reacts with H_2O and H_2 to form OH radical ($k_{H2O} = 2.2 \times 10^{-10}$ cm^3/sec, $k_{H2} = 1.0 \times 10^{-10}$ cm^3/sec). In addition, the H_2O in the cell serves to vibrationally cool the OH into its ground state ($k_{relax} = 1.4 \times 10^{-11}$ cm^3/sec). The ground state OH is probed via direct infrared absorption while it undergoes the chain reaction.

In addition to being an OH precursor, the H_2O serves to vibrationally cool any excited OH into its ground state.

$OH(v=1) + H_2O \rightarrow OH(v=0) + H_2O$ ($k_5 = 1.4 \times 10^{-11}$ cm^3/sec) (2.5)

The concentration of radicals in the flow tube is a linear function of excimer laser pulse energy and ozone concentration. In an effort to keep probability of radical-based side reactions to a minimum, the excimer pulse energy is kept as low as possible (~0.5 mJ/pulse), yielding a typical OH radical concentration of 1×10^{12} molecules/cm^3. Even assuming gas-kinetic rates for radical-radical reactions, the time scale for these reactions is on the order of 10 msec, which is at least an order of magnitude slower than the reaction of OH with ozone.

The temporal profile of the OH radical concentration is probed via an F-center laser, which is capable of continuous, single-mode operation[5] between 2.5 and 3.3 μm (4000 and 3030 cm^{-1}), with a linewidth of 2 MHz. In order to measure the frequency of the IR light, a portion of it is sent to a λ-meter (traveling Michelson interferometer) built after the design by Hall and Lee[6], using a polarization stabilized HeNe laser as a reference.

The temperature-controlled flow cell consists of an inner 106 cm long, 1" diameter quartz tube surrounded by a 3" diameter quartz jacket as shown in figure 2-3.

The temperature of the gas within the tube is maintained by pumping fluid between a heat-transfer coil and the outer jacket of the cell. Our current pumping system exchanges the fluid in the outer jacket every 15 seconds. Temperature within the cell is measured via a K type thermocouples (Chromel-Alumel) located just above the probe region of the inner tube. By using a transverse flow across the tube, temperature gradients are kept to a minimum $(0.5(5)^{o}$ C).

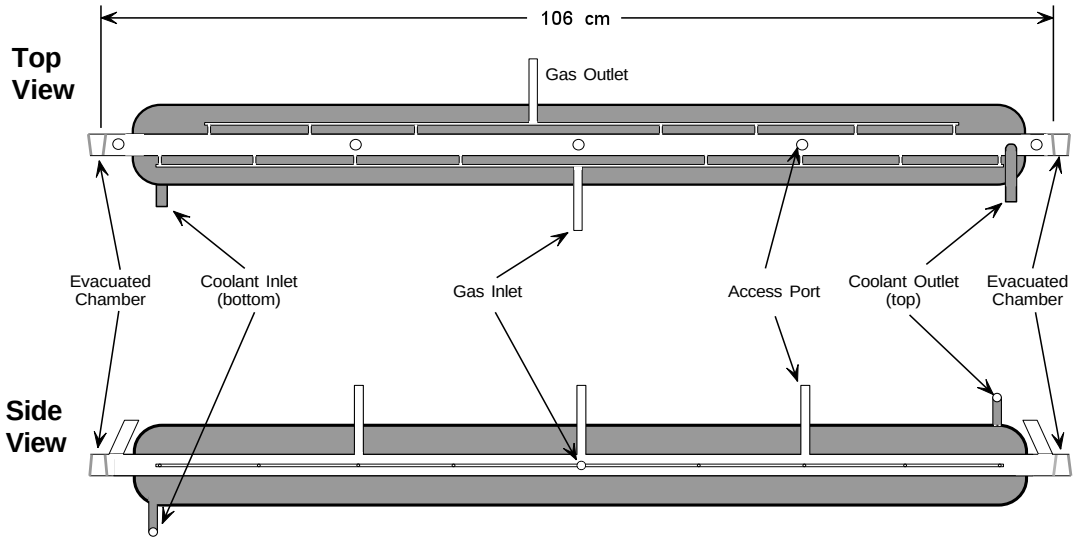

Figure 2-3. The temperature-controlled flow cell. The above figure shows the layout of the temperature-controlled flow cell. The gas inlet and outlet manifolds are designed such that gas flows across the cell (transverse flow). Transverse flow serves to reduce temperature and concentration gradients along the length of the cell. Surrounding the reaction chamber is a cooling jacket through which a temperature-controlled fluid is pumped. Also shown is the various access ports where we measure temperature and pressure of the gas.

Prior to entering the cell, the IR laser beam is split into two beams, which serve as signal and reference. The IR signal and excimer beams are overlapped via a 90% IR transmissive, 95% UV reflective dichroic mirror, and sent down the middle of the flow tube. The reference beam travels directly to the detector. The signal and reference beams are detected via 0.25 mm diameter, cryogenically-cooled InSb detectors. The detectors operate with a transimpedance of 50 kΩ and a bandwidth of 1 MHz. The resulting signals from the detector/amplifier combination are then sent to a differential amplifier, which allows subtraction of the common-mode noise. In addition, the reference signal is sent to an intensity stabilization servo, developed by Bill Chapman and Terry Brown[7]. This servo uses an electro-

optic (EO) modulator to vary the intensity of the Kr ion pump laser in an effort to cancel the noise on the reference detector. The combination of the intensity modulation servo and signal subtraction results in noise figures that are within a factor of 2 of the shot-noise limit, as shown in figure 2-4.

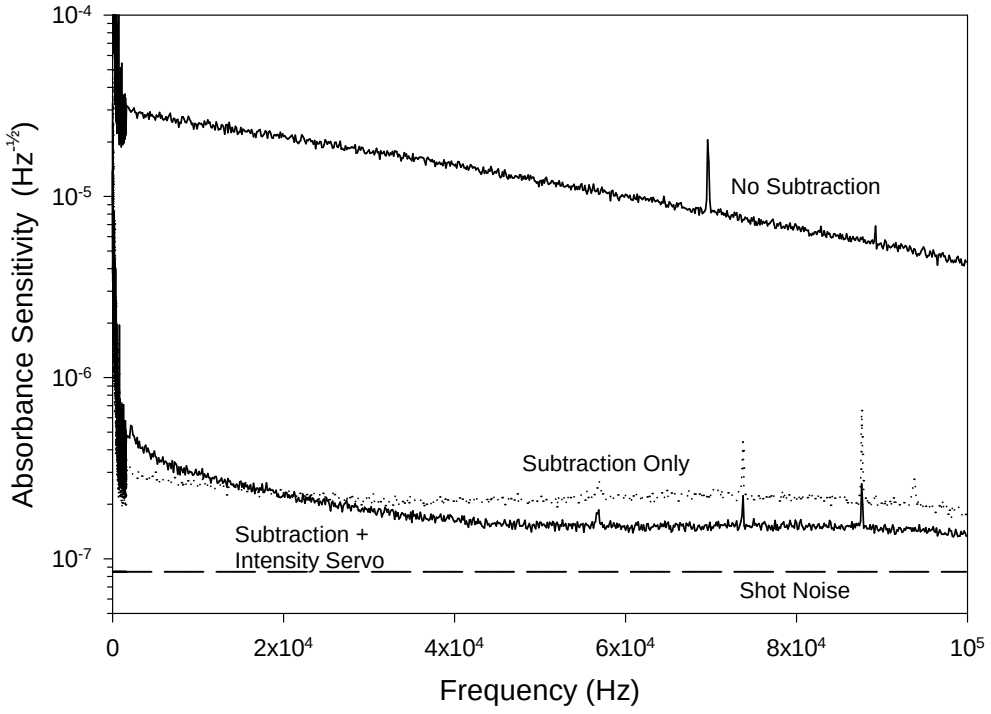

Figure 2-4. IR detection noise spectrum. The top trace shows the noise as viewed on a single detector. The intensity servo works to modulate the intensity of the Kr ion laser to cancel the noise on the reference InSb detector. The combination of this servo and signal subtraction puts our detection sensitivity to within a factor of two of the shot noise limit.

The subtracted signal is digitized and averaged with a 100 MHz digital oscilloscope. A typical data trace reflects approximately 250 averages. The averaged signal is transferred via a GPIB interface to a computer for storage and

analysis. The end result is an OH temporal profile with an absorption sensitivity of 2×10^{-8} $Hz^{-½}$.

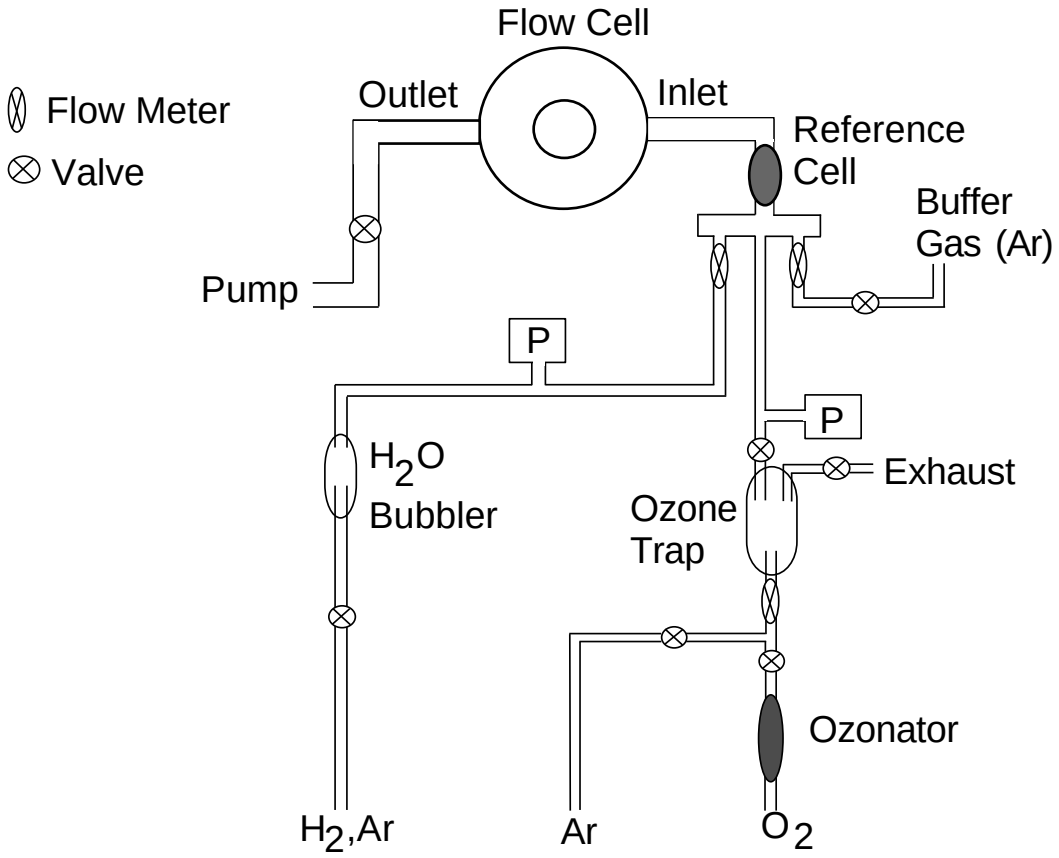

Figure 2-5. The gas handling system. Concentrations in the cell are proportional to their relative flow rates (equation 2.6), as measured by mass flow meters. Ozone is produced by an AC arc discharge (ozonator), and stored on silica gel at a temperature of ~200K. The absolute ozone concentration of the ozone is determined by 308nm absorption in the flow cell, and relative ozone concentration is measured by 254nm absorption in an 8.57 mm cell (reference cell). H_2O is added to the cell by flowing Ar or H_2 through a bubbler filled with H_2O. The fraction of H_2O present in the flow is determined by its vapor pressure at room temperature.

The various reactant and precursor gases are introduced into the flow cell by the gas handling system shown in figure 2-5. The concentrations are determined via their relative flow rates, which are measured by mass flow meters which are calibrated prior to the experiment by timing a pressure rise into a known volume. A

measured flow of Ar is passed through the ozone trap, where ozone is eluted into the Ar flow. A second gas flow into the flow cell is formed by passing Ar or H_2 gas through a porous frit immersed in a H_2O bubbler, which generates an H_2O concentration at the equilibrium vapor pressure, as shown in figure 2-6. At temperatures below 240K, however, we bypassed the H_2O bubbler and used a flow of pure H_2 to serve as the precursor gas. A third flow meter measures the flow of Ar buffer gas into the cell.

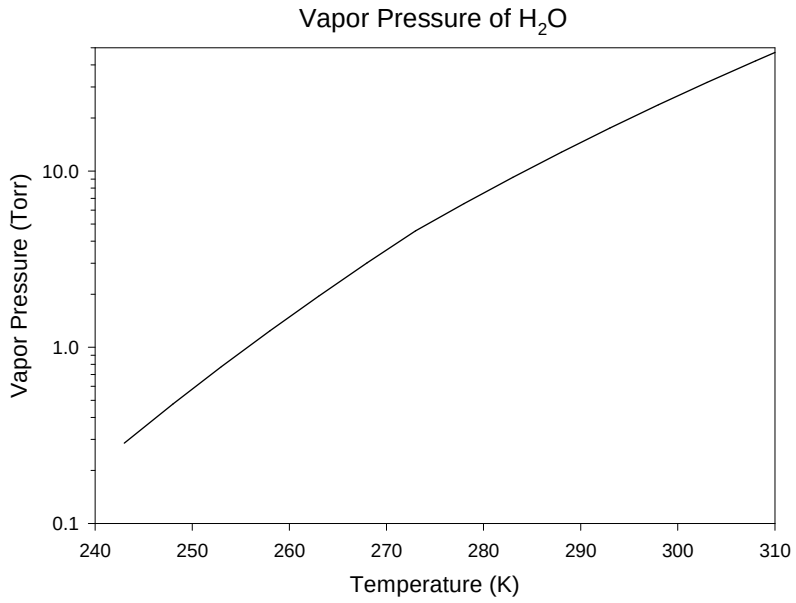

Figure 2-6. Vapor pressure of water as a function of temperature.

The partial pressure of each species in the cell is determined by the following equation:

$$P_i = \frac{f_i \chi_i}{\sum_i f_i} P_{TOT}, \qquad (2.6)$$

where f_i is the flow rate as measured by the particual mass flow meter, χ_i is the fraction of the species present within the particual flow, and P_{TOT} is the total pressure in the flow cell as measured by a 100 Torr Baratron gauge.

Ozone is produced in an AC discharge from molecular oxygen (99.99%) and adsorbed in a pyrex cylinder filled with silica gel at approximately -110° C.[8,9] Prior to entering the flow tube, the concentration of ozone is determined by absorption of the Hg emission line at 253.7 nm in a calibrated 8.56 mm transmission cell, based on the known absorption cross section [10-12] of $\sigma = 1.137 \times 10^{-17}$ cm^2. In addition, the absolute concentration of ozone is measured in situ via 308 nm UV absorption. Because of the important role the absolute concentration of ozone plays in the determination of the rate constant, it is of utmost importance that the measurement be accurate. For this reason, we utilize the *in situ* ozone concentration measurement to determine the absolute ozone density. In order to do this properly, we must take into account subtle experimental factors, such as the proper emission wavelengths of the XeCl excimer and the temperature dependence of the ozone cross section at 308 nm. The ozone UV cross section is calculated using a weighted average of the two XeCl emission lines (307.9 nm and 308.2 nm) with their proper 2:5 integrated intensity ratio.[13] We also corrected the ozone cross section at these wavelengths for their temperature dependence, as shown in figure 2-7.[14,15]

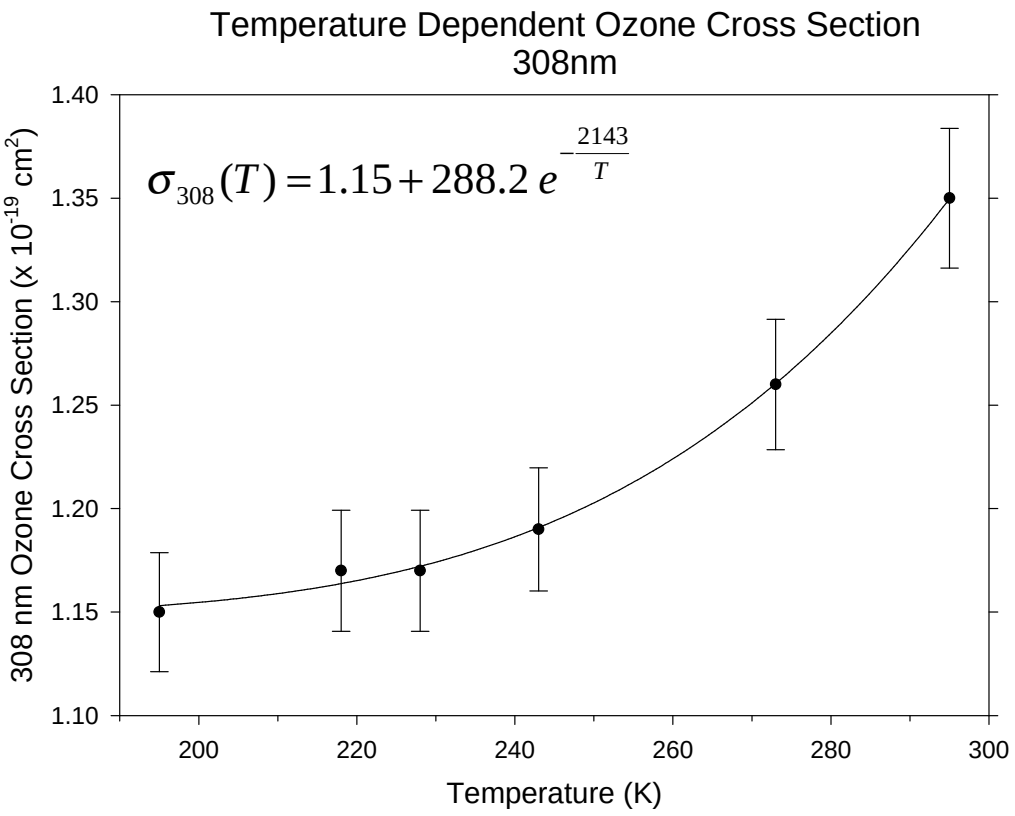

Figure 2-7. Temperature dependence of the ozone cross section[14,15] at 308 nm. Each cross section is based on the XeCl emission lines at 307.9 and 308.2 nm, with a 2:5 integrated intensity ratio.

In order to properly interpolate the cross section between measured temperatures, the data is fit to an exponential form given by

$$\sigma_{308}(T) = A + B\, e^{-\frac{C}{T}}, \qquad (2.7)$$

where A = 1.15 x 10^{-19} cm^2, B = 288 x 10^{-19} cm^2, and C = 2143 K. This form is chosen to reflect a simple "Arrhenius-type" expression. That is, at any given temperature, the probability of absorption of 308nm light by an ozone molecule is given by $e^{\frac{-C}{T}}$. As T increases to infinity, σ_{308} becomes A + B, and as T decreases to zero, σ_{308} goes to A. A table of the 308 nm ozone UV cross sections as well as the

corresponding quantum yields for $O(^1D)$ (Φ)at various temperatures appears in table 2-1.

Temperature (K)	$\sigma^{308}[O_3]$ ($10^{-19}cm^2$)	$\Phi^{308}[O_3]$ (%)
334	[1.62(8)]	[81]
314	[1.46(7)]	[81]
295	1.35(3)	81
287	1.31(3)	80
273	1.26(3)	76
266	1.24(3)	74
253	1.21(3)	68
250	1.20(3)	66
240	1.19(3)	60

Table 2-1. The temperature dependant cross section[14,15] (σ) and quantum yield[4] (Φ) for ozone at 308nm. The numbers in braces represent extrapolation from measured quantities.

2.3 The Temperature-Controlled Flow Cell

The temperature-controlled flow cell used for these experiments is shown in figure 2-3. The tube is made entirely of quartz, and consists of a gas inlet/outlet manifold, reaction chamber, and cooling jacket.

The reaction chamber is a tube 106 cm long, 2.5 cm in diameter, with a volume of 0.56 L. The ends of the chamber are made of IR grade, quartz optics, with a transmittance of >90% in both the IR and UV. Each end of the reaction chamber has a set of such optics, separated by an evacuated chamber. This evacuated chamber, positioned outside the cooling jacket, serves to protect the optics from condensation at low temperatures. Each optic is tilted at approximately 5° from normal to minimize interference effects due to reflections from the surface. The reaction chamber possesses three observation ports, allowing measurement of

parameters such as temperature and pressure. In addition, there are two ports, on either end of the cell, that allow cleaning of the interior surface of the optics.

Gas enters and leaves the reaction chamber through the gas inlet/outlet manifold. The gas inlet system runs the entire length of the tube, allowing fresh gas to flow into each area of the chamber. Offset from these inlet ports are the outlet ports, though which the gas is pumped away. The result is a net flow *across* the reaction chamber that serves to reduce concentration and temperature gradients of the reactants and products along the length of the cell. The rate of this flow is determined by the total rate of flow into and out of the tube, but under typical conditions, the reaction chamber is refreshed every 10 seconds.

The cooling jacket surrounds the gas inlet/outlet systems and the reaction chamber. The jacket contains a fluid, whose temperature is varied externally via a heat-exchanger apparatus. The fluid is circulated by a 32 L/min pump between the cooling jacket of the flow cell and a copper heat-exchanger coil, immersed in a constant temperature bath. At this pumping speed, the fluid in the cooling jacket is refreshed every 15 seconds.

The choice of fluids used in the heat-exchanger bath and the cooling jacket is dictated by the temperature that one wishes to achieve. It is imperative that the freezing point of the fluid used in the cooling jacket be lower than that of the heat-exchanger bath. Otherwise, freezing of the fluid might occur, causing damage to the flow tube. A table of various fluids and their freezing points are contained in table 2-2.

Fluid	Freezing Temperature (C)
Water	0
Ethanol	-115
Pentane	-130

Table 2-2. The freezing point for various fluids used to cool the cell.

2.4 The Questek Excimer Laser

Performance of the Questek 2000 series excimer laser is dependant on two factors: (1) gas purity, and (2) electrode conditions. Gas purity is a general concern, especially when switching the excimer from a chlorine-based mixture to a fluorine-based mixture. The Questek manual describes a procedure for successfully changing gas mixtures, but experience has shown that it is necessary to open the chamber and physically clean all surfaces. In addition, multiple fluorine passivation cycles must be performed before the laser operates reliably.

Electrode and discharge conditions play an important role in the operation of the laser. If proper safety precautions are taken, it is possible to view the discharge using a reasonably thick piece of plexi-glass (1” - 2” thick). However, if there is a non-lasing mix in the chamber, it is possible to view the discharge with a pair of lab safety glasses. During the discharge, one should see an even glow between the two electrodes. The discharge should be free of any sparks, or “lightning bolts”, between the electrodes, which will eventually damage its surface. If these sparks are visible, it may indicate uneven spacings between the pre-ionization pins located on either side of the electrode assembly. The pre-ionization pin spacing is 0.040”, which is much smaller than the 0.740” spacing of the electrodes. Hence, a small

electric discharge occurs between the pins, catalyzing the breakdown between the electrodes. These pre-ionization gaps increase over time, due to the harsh environments to which they are constantly exposed. When this occurs, it is necessary to readjust or replace the pins. Prolonged exposure to improper breakdown conditions will cause the electrodes to become pitted. Because the electrodes are made of solid nickel, they can be polished. However, one must take care to preserve the slight bow along the length of its surface.

2.5 The Kr Ion Laser

The Kr ion laser acts as a pump laser for the F-center laser. In order to insure reliable operation of the Kr ion laser, constant attention and care are required. In order to more fully understand the operation of the ion laser, a block diagram outlining the major components is included in figure 2-8.

In order to pump the F-Center laser properly, it is necessary to have at least one Watt of output power. This value of one Watt originates from the 800 mWatts needed to pump the F-Center laser plus an extra 20% to make up for loss from the intensity servo. If the Kr ion laser cannot achieve this power, the most likely cause is overpressure of Kr in the tube. As the pressure in the tube increases, the effective resistance of the tube increases. Therefore, for a given tube voltage, the current will decrease as the effective resistance increases. In order to recover the lost power, one must either increase the voltage or decrease the pressure. Increasing the voltage on the laser tube is achieved by adjusting the taps on the auto-transformer in the power supply. A table containing laser tube voltage and tap positions is shown in table 2-3.

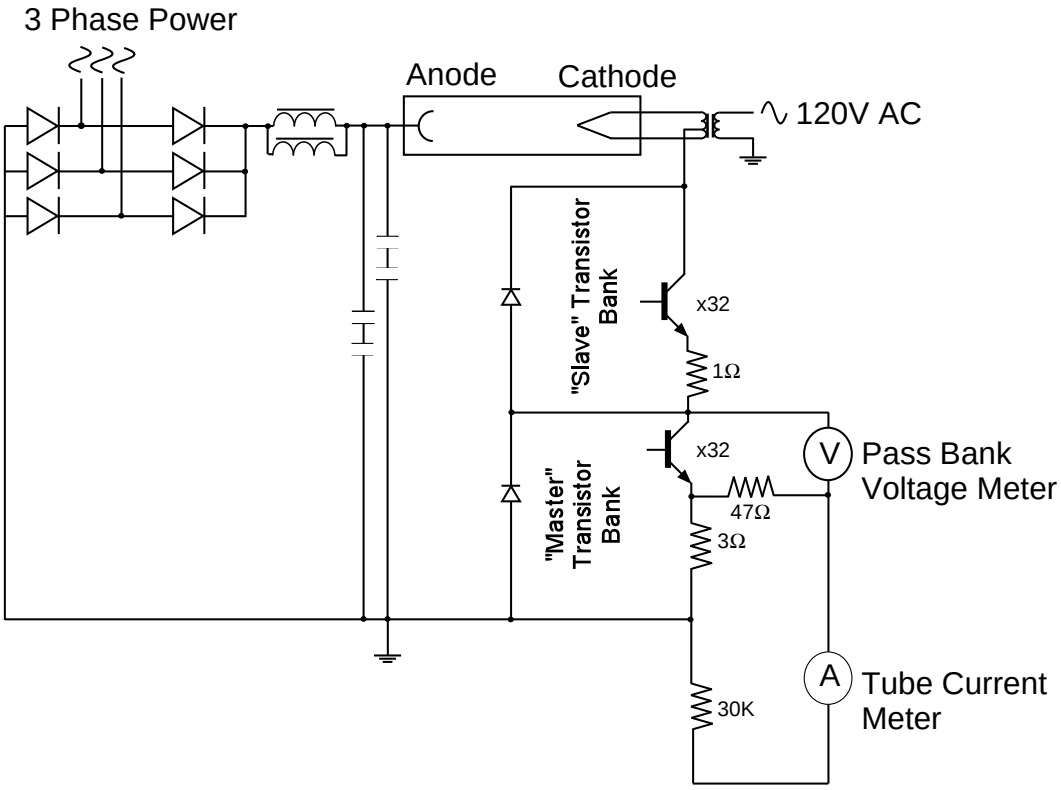

Figure 2-8. Block diagram of the Kr ion laser.

Tap Position (Primary lead = 9)	Tube Voltage (Volts)
1	435
2	460
3	485
4	510
5	540
6	560
7	575
8	600

Table 2-3. Kr ion laser tube voltage at various auto-transformer tap positions

The pressure of the laser tube can be measured via the Hastings TC gauge located near on the cathode end of the ballast reservoir. Unfortunately, we do not have a Hastings TC gauge reader. We have calibrated one of the ubiquitous Varian

801 TC gauge readers in the lab in order to read the actual pressure in the tube. This calibration curve is contained in figure 2-9. The optimum Kr pressure in the tube is 150 mTorr (180 mTorr as read by Varian 802 gauge). If the pressure in the tube is 50% greater than optimum, it is necessary to pump the laser tube down to its optimum pressure.

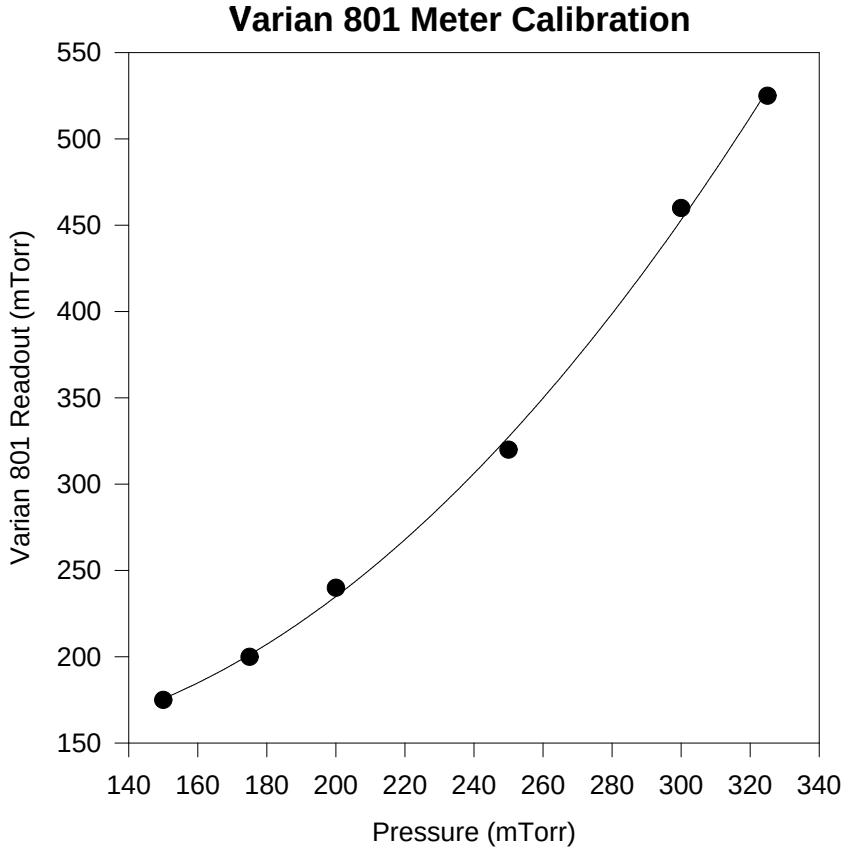

Figure 2-9. Calibration of the Varian 801 meter reading a Hastings TC gauge. Optimum tube pressure is 150 mTorr, which reads as approximately 180 mTorr on the Varian 801 gauge. The data above is fitted to a 2^{nd} order polynomial with the following coefficients: a[0] = 197.3, a[1] = -1.141, a[2] = 6.644×10^{-3}.

Pumping the laser tube is very risky, and great care must be taken to insure the purity of the Kr is not compromised. All tubing must be clean, and all joints must be vacuum tight. A liquid-nitrogen trapped, diffusion pump system works especially well. Due to the small orifice of the Nupro valve on the Kr ion laser tube, overloading the diffusion pump is not a concern. Typically, it takes approximately 20 minutes to reduce the pressure in the Kr laser tube by 50 mTorr.

The transistor bank serves to regulate the current through the laser tube by limiting the tube voltage. Because of the high currents (~40 Amps) and voltages (~500 V), the regulating transistors must work in parallel, dividing the voltage and current between them. The most common failure mode of the laser is the shorting of one or more transistors in the "Master" or "Slave" power transistor bank. When this occurs, it is necessary to find the "blown" transistor and replace it.

The test circuit for the "Master" transistor bank is shown in figure 2-10.

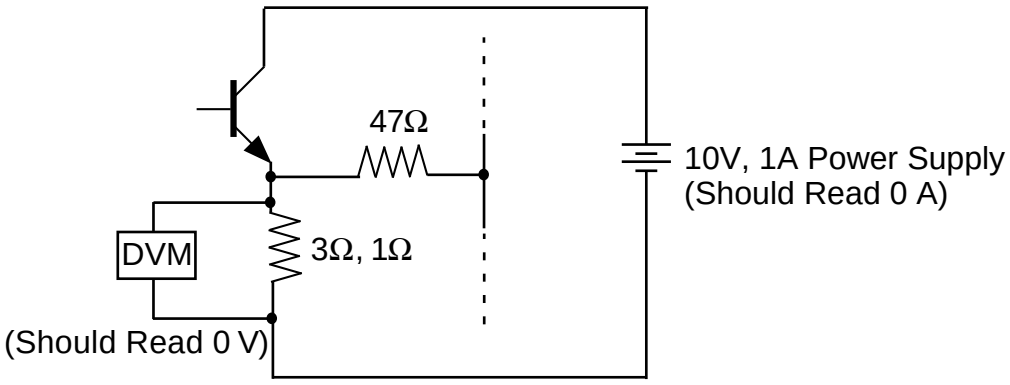

Figure 2-10. Test circuit for the "Master" and "Slave" transistor banks. When testing the "Slave" bank, it is also necessary to disconnect the driver transistor. A properly working transistor bank should sink very little current, and the voltage drop over the 3Ω (1Ω for "Slave") should be negligible.

Using a ~1A current limiting power supply, connect the positive lead to the transistor's collector, and the ground lead to the 3 Ohm resistor. If the transistor is blown, the power supply current should read its limiting value, and the voltage drop over the 3 Ohm resistor should be the voltage difference between the leads. A properly working power transistor bank should sink very little current (~50 mA), and the voltage drop over the 3 Ohm resistor should be 0 Volts.

The procedure for testing the "Slave" transistor bank is very similar to the above procedure. However, it is necessary to first disconnect the small driver transistor (not shown in block diagram). If you do not disconnect this driver transistor, the "Slave" bank will sink current even if working properly. After disconnecting the driver transistor, the "Slave" transistor bank can be tested in the same manner as the "Master" transistor bank (see test circuit in figure 2-10).

References for Chapter 2

1 D. D. Nelson Jr, A. Schiffman, and D. J. Nesbitt, *J. Chem. Phys.* **93,** 7003 (1990).

2 A. Schiffman and D. J. Nesbitt, *J. Chem. Phys.* **95,** 2629 (1991).

3 A. Schiffman and D. J. Nesbitt, *J. Chem. Phys.* **100,** 2677 (1994).

4 W. B. DeMore, S. P. Sander, D. M. Golden, R. F. Hampson, M. J. Kurylo, C. J. Howard, A. R. Ravishankara, C. E. Kolb, and M. J. Molina, (Jet Propulsion Laboratory, Pasadena, California, 1994).

5 A. Schiffman, D. D. Nelson Jr., M. S. Robinson, and D. J. Nesbitt, *J. Phys. Chem.* **95,** 2629 (1991).

6 J. L. Hall and S. A. Lee, *Appl. Phys. Lett.* **29,** 367 (1976).

7 W. B. Chapman, , University of Colorado, Boulder, 1997.

8 E. Coleman, T. Siegrist, D. A. Mixon, P. L. Trevor, and D. J. Trevor, *J. Vac. Sci. Technol.* **A9,** 2408 (1991).

9 G. A. Cook, A. D. Kiffer, C. V. Klumpp, A. H. Malik, and L. A. Spence, *Ozone Chemistry and Technology* (American Chemical Society, Washington, 1959).

10 K. J. Mauersberger, D. Hanson, and J. Morton, *Geophys. Res. Lett.* **13,** 671 (1986).

11 A. G. Hearn, *Proc. Phys. Soc. London* **78,** 932 (1961).

12 G. Brasseur and S. Solomon, *Aeronomy of the Middle Atmosphere* (Reidel, Dordrecht, 1986).

13 G. Mount, *J. Geophys. Res.* **97,** 2427 (1992).

14 J. Brion, A. Chakir, D. Daumont, J. Malicet, and C. Parisse, *Chem. Phys. Lett.* **213,** 610 (1993).

15 D. Daumont, J. Brion, J. Charbonnier, and J. Malicet, *J. Atmos. Chem.* **15,** 145 (1992).

CHAPTER 3

DATA AND RESULTS

3.1 Kinetic Analysis

The chemical chain process is initiated by pulsed laser photolysis of O_3 at 308 nm, thus creating $O(^1D)$ atoms. These excited $O(^1D)$ atoms rapidly react with water[1-3] and hydrogen[4-7] in the flow cell to yield both vibrationally "hot" (i.e., v>0) and "cold"(i.e., v=0) OH radicals. These studies[1-3] have shown that the ratio of OH(v=1) to OH(v=0) resulting from reaction 3.1 is approximately 0.40. In addition, studies[4-7] of the OH vibrational distribution resulting from reaction 3.3 have shown a distribution in which 80% of the OH population is in $v \geq 7$.

$O(^1D) + H_2O \rightarrow OH + OH$ $\quad k = 2.2 \times 10^{-10}$ cm^3/sec (3.1)

$O(^1D) + H_2 \rightarrow OH + H$ $\quad k = 1.0 \times 10^{-10}$ cm^3/sec (3.2)

$H + O_3 \rightarrow OH + O_2$ $\quad k = 2.9 \times 10^{-11}$ cm^3/sec (3.3)

There is also rapid competition to quench or react the $O(^1D)$ species with O_3 (k =2.4 x 10^{-10} cm^3 molecule^{-1} s^{-1}) or O_2 (k = 3.2 x 10^{-11} cm^3 molecules^{-1} s^{-1}) to yield ground state oxygen atoms or molecules via[8-10]

$O(^1D) + O_3 \rightarrow 2\ O_2$ $\quad k = 1.2 \times 10^{-10}\ cm^3/sec$ (3.4)

$O(^1D) + O_3 \rightarrow O_2 + 2\ O(^3P)$ $\quad k = 1.2 \times 10^{-10}\ cm^3/sec$ (3.5)

$O(^1D) + O_2 \rightarrow O_2 + O(^3P)$ $\quad k = 4.0 \times 10^{-11}\ cm^3/sec$ (3.6)

Since the high-resolution IR laser samples on $P(5/2)1^-$ transitions out of OH (v=0, J=2.5), the early time signals reflect only the fraction of vibrationally "cold" OH radicals. Rovibrational cooling of the "hot" OH species by collisions with H_2O and Ar buffer gas rapidly brings the system to room temperature equilibration. Under typical flow cell conditions, rapid quenching of these rovibrationally "hot" OH radicals, results in an essentially "prompt" rise in OH signals probed out of the v = 0, low N quantum levels, which on a much longer timescale, reacts with O_3 to initiate the chemical chain reaction cycle (see figure 3-1). The key point is that the OH populations are equilibrated to a temperature distribution on <5 μs time scale, which is 1 or 2 orders of magnitude faster than the subsequent chain reaction kinetics under investigation.

Thus, for the purposes of kinetic analysis, initiation of the chain reaction can be approximated simply by prompt generation of $[OH]_0$ at t = 0. For typical XeCl pulse energies and beam sizes, $[OH]_0$ is 3 or 4 orders of magnitude smaller than $[O_3]$,which is necessary to ensure a pseudo-first-order kinetic regime and discriminate against radical-radical termination reactions. In this limit, the relevant coupled kinetic equations become

$$\frac{d[OH]}{dt} = -k_1[OH][O_3] + k_2[HO_2][O_3] \quad (3.7)$$

$$\frac{d[HO_2]}{dt} = k_1[OH][O_3] - k_2[HO_2][O_3] \quad (3.8)$$

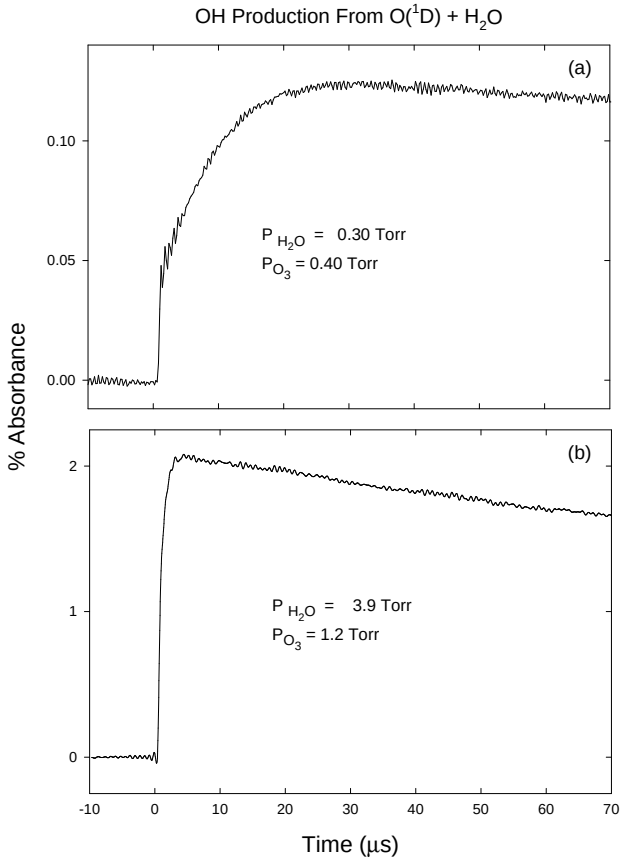

Figure 3-1. OH time profiles measured via time-resolved IR laser absorption on the v=1←0, P(2.5)1$^-$ transition. In a and b, the buffer gas conditions are chosen to modify the rate of collisional relaxation of the OH radicals, which in effect samples the early time scale dynamics for OH production. (a) At the lowest H_2O quenching gas concentrations, there is a "prompt" component of OH(v=0) absorption due to rapid reaction of $O(^1D)$ with H_2O, which then rises to roughly twice this value with subsequent collisions in the buffer gas. This nearly 2-fold additional increase in OH signal reflects that vibrationally "hot" (i.e., v > 0) and "cold" OH(v=0) radicals are generated in roughly equal numbers, corresponding to "active" and "spectator" OH bonds in the $O(^1D) + H_2O$ reaction. (b) For typical H_2O concentrations, however, this collisional relaxation is too rapid to distinguish these two components. The net effect is a prompt production of collisionally equilibrated OH radicals on the 5 μs time scale, which is much faster than the subsequent $OH/HO_2/O_3$ chain reaction kinetics of interest.

$$\frac{d[\mathrm{OH}]}{dt} + \frac{d[\mathrm{HO_2}]}{dt} = 0, \tag{3.9}$$

where the last expression reflects the neglect of any net loss of chain radical concentration due to slow wall losses, diffusion out of beam, etc. These kinetic equations can be readily solved for [OH](t) and [HO_2](t) to yield

$$\frac{[\mathrm{OH}](t)}{[\mathrm{OH}]_0} = \frac{k_1}{k_1 + k_2} e^{-k_{\mathrm{ind}}[\mathrm{O_3}]t} + \frac{k_2}{k_1 + k_2} \tag{3.10}$$

$$\frac{[\mathrm{HO_2}](t)}{[\mathrm{OH}]_0} = \frac{k_1}{k_1 + k_2} \left(1 - e^{-k_{\mathrm{ind}}[\mathrm{O_3}]t}\right), \tag{3.11}$$

where the effective chain induction rate and steady-state concentrations of OH radical and steady-state rate of chain propagation are given by

$$k_{\mathrm{ind}} = k_1 + k_2 \tag{3.12}$$

$$[\mathrm{OH}]_{\mathrm{ss}} = [\mathrm{OH}]_0 \frac{k_2}{k_1 + k_2} \tag{3.13}$$

$$k_{\mathrm{prop}} = \frac{k_1 k_2}{k_1 + k_2}[\mathrm{O_3}]. \tag{3.14}$$

Equation (3.10) for the time dependence of [OH] illustrates several important points. First of all, [OH](t) starts initially at $[OH]_0$ and undergoes single-exponential decay to a nonzero baseline value of $[\mathrm{OH}]_{\mathrm{ss}} = [\mathrm{OH}]_0 \frac{k_2}{k_1 + k_2}$, with a chain "induction" time constant $\tau_{\mathrm{ind}} = \{k_{\mathrm{ind}}[\mathrm{O_3}]\}^{-1}$. This induction time constant reflects the time required for OH and HO_2 radicals to come into steady state, and therefore is controlled by the magnitude of *both* chain propagation steps. Consequently, any kinetic analysis of this exponential time dependence yields the *sum* of the two pseudo-first-order propagation rate constants, k_1 and k_2. This is different from previous kinetic analyses[11-13] of OH + O_3 reaction rates, which

neglect the slower second chain step and ascribe the observed time dependence entirely to $1/\tau_{ind} \approx k_1[O_3]$. Secondly, the OH decays to a *nonzero value* at $t >> \tau_{ind}$ due to chain regeneration of OH from the secondary $HO_2 + O_3$ reaction. This also differs from previous analyses of $OH + O_3$ kinetics, which treat the OH signal as a *single* exponential decay down to $[OH]_{ss} \approx 0$ and ascribe this time constant to the first step in the chain reaction sequence. Sample chain reaction data supporting this more complete kinetic analysis are presented in figure 3-2, where the water and ozone reagent concentrations are listed in the figure caption.

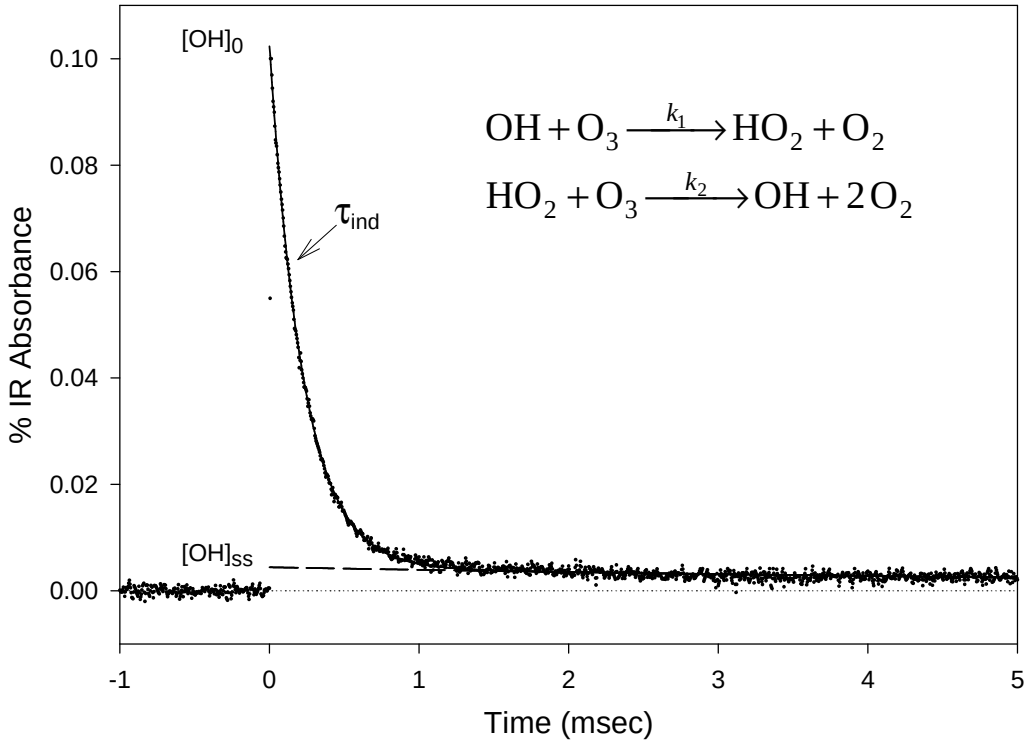

Figure 3-2. Typical OH absorbance data. The fast initial decay signals the "induction" of the chain reaction, followed by a much slower decay from the steady state "propagation" regime to chain termination processes. The fast decay is determined by the sum of the two chain rate constants, whereas the ratio of fast- to slow-decay components reflects the ration of the two chain rate constants. For this data, $[O_3]$ = 1.95 Torr, $[H_2O]$ = 5.22 Torr, [Ar] = 19 Torr, and the excimer pulse energy is 0.5 mJ/cm^2 per pulse.

As predicted, the data unambiguously demonstrates single exponential decay from $[OH]_0$ to a *finite* $[OH]_{ss}$ plateau, which in turn decays on a much longer time scale ($t_{decay} \geq 10$ ms) due to a combination of nonlinear chain termination and diffusion out of the probe laser IR beam volume. Though this secondary decay is due to chain termination and therefore not predicted by the simple chain model, it can be easily treated by including *irreversible* (i.e., non-chain reaction sustaining) loss processes for OH and HO_2, as presented below.

If we assume first-order, irreversible loss mechanisms for OH and HO_2 radicals, the relevant kinetic equations are modified to become

$$\frac{d[OH]}{dt} = -k_1[OH][O_3] + k_2[HO_2][O_3] - k_{irr}^{OH}[OH], \quad (3.15)$$

$$\frac{d[HO_2]}{dt} = k_1[OH][O_3] - k_2[HO_2][O_3] - k_{irr}^{HO_2}[HO_2], \quad (3.16)$$

$$\frac{d[OH]}{dt} + \frac{d[HO_2]}{dt} = -k_{irr}^{OH}[OH] - k_{irr}^{HO_2}[HO_2]. \quad (3.17)$$

Efficient propagation occurs when irreversible loss of OH and HO_2 is *slow*, and thus the chain reaction is sustained for many cycles. This is kinetically equivalent to saying that the OH/HO_2 ratio is maintained in a steady-state ratio k_2/k_1, even as both chain radical species are eventually consumed irreversibly. In this simplifying limit of k_{irr}^{OH}, $k_{irr}^{HO_2} << k_{ind}$, equations (3.15-3.17) can be solved to yield

$$\frac{[OH](t)}{[OH]_0} = \frac{k_1}{k_1 + k_2} e^{-k_{ind}[O_3]t} + \frac{k_2}{k_1 + k_2} e^{-k_{term}t}. \quad (3.18)$$

This now correctly predicts a *double*-exponential decay in the OH signal, with the faster chain induction component given by k_{ind} and a slower chain *termination* component given by

$$k_{\text{term}} = \frac{k_{\text{irr}}^{\text{OH}}\, k_2}{k_1 + k_2} + \frac{k_{\text{irr}}^{\text{HO}_2}\, k_1}{k_1 + k_2}\,. \qquad (3.19)$$

It is interesting to note from equation 3.18 that the chain termination rate reflects a *sum of both* OH and HO_2 loss rates, but now weighted by the fractional steady-state concentrations of each radical. As a result, these $OH/HO_2/O_3$ chains can still propagate quite efficiently even in the presence of relatively fast irreversible removal processes for OH, due simply to the fact that the *overall* concentration of chain radicals (i.e., $[OH] + [HO_2]$) is "stored" as the less reactive HO_2 radical. Note also that this model predicts the *ratio* of k_1/k_2 to be determined by the relative amplitudes of the fast- and slow-decay components back extrapolated to $t = 0$. Finally, the total number of chain cycles is typically dominated by the long time propagation behavior, which can be found by integration of equation (3.18) to yield

$$N_{\text{cycles}} \approx \frac{k_{\text{prop}}}{k_{\text{term}}} = \frac{k_1 k_2 [\text{O}_3]}{k_{\text{irr}}^{\text{OH}} k_2 + k_{\text{irr}}^{\text{HO}_2} k_1}\,. \qquad (3.20)$$

In summary, the above kinetic analysis makes three predictions. (1) In the limit of efficient chain propagation and slow chain termination processes, double-exponential time dependence of the OH chain radicals is anticipated. (2) A plot of the fast decay rate vs $[O_3]$ will yield a slope of $\{k_1 + k_2\}$ (i.e., the *sum* of the two chain propagation reaction rate constants). (3) The ratio of back extrapolated components for fast (induction) and slow (termination) decays yields k_1/k_2 (i.e., the ratio of the two chain propagation rate constants). A table of relevant reactions occurring in the flow cell are presented in table 3-1.

Reaction	k[298K] (cm^3/sec)	Reference
$O(^1D) + H_2 \rightarrow OH + H$	1.0×10^{-10}	14
$O(^1D) + H_2O \rightarrow OH(v=1) + OH(v=0)$	2.2×10^{-10}	2
$O(^1D) + O_2 \rightarrow O + O_2$	4.0×10^{-11}	14
$O(^1D) + O_3 \rightarrow 2\ O_2$	1.2×10^{-10}	14
$O(^1D) + O_3 \rightarrow O_2 + 2\ O$	1.2×10^{-10}	14
$H + O_3 \rightarrow OH(v\leq 9) + O_2$	2.9×10^{-11}	4-7
$OH(v=1) + H_2O \rightarrow OH(v=0) + H_2O$	1.4×10^{-11}	15
$OH(v=1) + H_2 \rightarrow OH(v=0) + H_2$	1.0×10^{-14}	16
$OH(v=1) + O_2 \rightarrow OH(v=0) + O_2$	1.3×10^{-13}	17,18
$OH(v=2) + Ar \rightarrow OH(v=1) + Ar$	$<1.0 \times 10^{-14}$	19
$OH(v=2) + O_3 \rightarrow HO_2 + O_2$	1.9×10^{-12}	20,21
$OH + O_3 \rightarrow HO_2 + O_2$	8.2×10^{-14}	13
$HO_2 + O_3 \rightarrow OH + 2\ O_2$	2.1×10^{-15}	22
$HO_2 + O \rightarrow OH + O_2$	5.9×10^{-11}	14
$OH + O \rightarrow O_2 + H$	3.3×10^{-11}	14
$O_3 + O \rightarrow 2\ O_2$	8.0×10^{-15}	14
$OH + OH \rightarrow H_2O + O$	1.9×10^{-12}	14
$OH + HO_2 \rightarrow H_2O + O_2$	1.1×10^{-10}	14
$HO_2 + HO_2 \rightarrow$ products	1.7×10^{-12}	14
$OH + H_2 \rightarrow H_2O + H$	6.7×10^{-15}	14

Table 3-1. Reactions occurring in the flow cell and their respective rate constants.

3.2 Room Temperature Results

To obtain the desired kinetic rate information, time-resolved IR absorption traces for loss of OH radical after excimer laser initiation are obtained for a wide variety of experimental conditions. To verify that the kinetic results are quantitatively reliable, these experiments have been exhaustively repeated for ≈140 different cell pressures, buffer gases, flow rates, photolysis energies, and over a 100-

fold dynamic range of ozone concentrations. An abbreviated list of the experimental conditions is summarized in table 3-2.

No. of Data Runs	Laser Energy (mJ cm^{-2} $pulse^{-1}$)	H_2 Pressure (Torr)	H_2O pressure (Torr)	Total Pressure (Torr)	$[O_3]$ x 10^{16} molecules/cm^3	k_{ind} (10^{-14} cm^3/sec)
19	7.5	0	5.0	45.0	0.097 – 9.46	8.2(8)
21	4.3	0	6.6	34.9	0.25 – 7.56	8.7(8)
6	5.0	0	5.3	29.7	0.13 – 1.16	9.2(9)
21	4.9	0	4.0	24.6	0.20 – 6.45	8.3(8)
21	2.8	0	1.3	42.5	0.47 – 7.62	9.1(9)
20	1.6	0	3.3	23.4	0.42 – 6.69	8.7(8)
12	2.4	0	6.0	16.7	0.50 – 4.59	11.0(11)
19	2.6	0	12.5	43.4	0.095 – 4.52	8.0(8)
10	0.5	0	3.7	26.0	0.25 – 2.00	8.6(9)
23	0.4	0	3.8	28.0	0.50 – 3.95	8.3(8)
21	0.5	0	3.1	23.0	0.45 – 3.95	8.6(9)
18	0.5	0	3.7	27.0	0.60 – 4.05	9.3(9)
14	0.5	0	3.6	22.0	0.73 – 2.41	9.4(9)
12	0.5	1.4	0.4	26.0	0.19 – 4.00	9.2(9)
8	0.5	0	0.6	18.0	0.85 – 8.41	8.7(9)
22	0.5	12.0	3.0	25.0	0.94 – 6.52	8.7(9)
10	0.5	8.3	1.2	23.0	0.57 – 6.34	8.3(9)
8	0.5	10.0	2.8	22.0	1.02 – 5.00	8.7(9)
10	0.5	6.7	3.3	17.5	0.73 – 6.50	9.9(10)
15	0.5	0	0.5	25.0	1.00 – 6.87	10.0(10)

Table 3-2. Experimental conditions for room temperature determination of k_{ind}.

A more complete discussion of these various experimental checks is deferred until later in this section. Each OH radical time trace is then fitted to the double exponential decay form predicted in equation (3.18) using nonlinear least-squares routines to extract k_{ind}, k_{term} and the ratio of the fast- and slow-decay components. Sample-fitted data are shown in figure 3-2, which indicate the high signal-to-noise (S/N) quality and small residuals obtained from the least-squares-fitting procedure.

From equation (3.20), these experimental conditions support over 20 complete chain cycles (i.e., more than 40 molecules of O_3 are destroyed for each OH radical generated photolytically). The chain induction rate component (k_{ind}) has been plotted vs ozone concentration in figure 3-3.

From a linear least-square analysis, the slope of this fit (i.e., the induction rate constant) at 298 K is $k_{ind} = k_1 + k_2 = 8.8(9) \times 10^{-14}$ cm^3 molecule^{-1} s^{-1} , with an intercept which is negligible within uncertainty. It is worth stressing that these data reflect the results of ≈200 separate kinetic measurements, taken at over a 50-fold dynamic range in laser pulse energies and cell pressures, as well as over a 100-fold dynamic range in $[O_3]$.

Though such chain reaction kinetics have been present in previous experimental studies, the effects require relatively high S/N to see unambiguously. Furthermore, detection of the steady state chain regime is enhanced by the higher ozone concentrations accessible to the present IR method, which is able to make the initial decay rapid with respect to radical-radical chain termination processes and diffusion out of the probe beam. This is the first kinetic study of the $OH/HO_2/O_3$ reaction system that takes chain propagation effects explicitly into account, and which therefore reports the sum of the two chain rate constants (i.e., $k_{ind} = k_1 + k_2$). By way of contrast, previous kinetic analyses have approximated the loss of OH as a single-exponential function of time and report a value for k_1 alone.

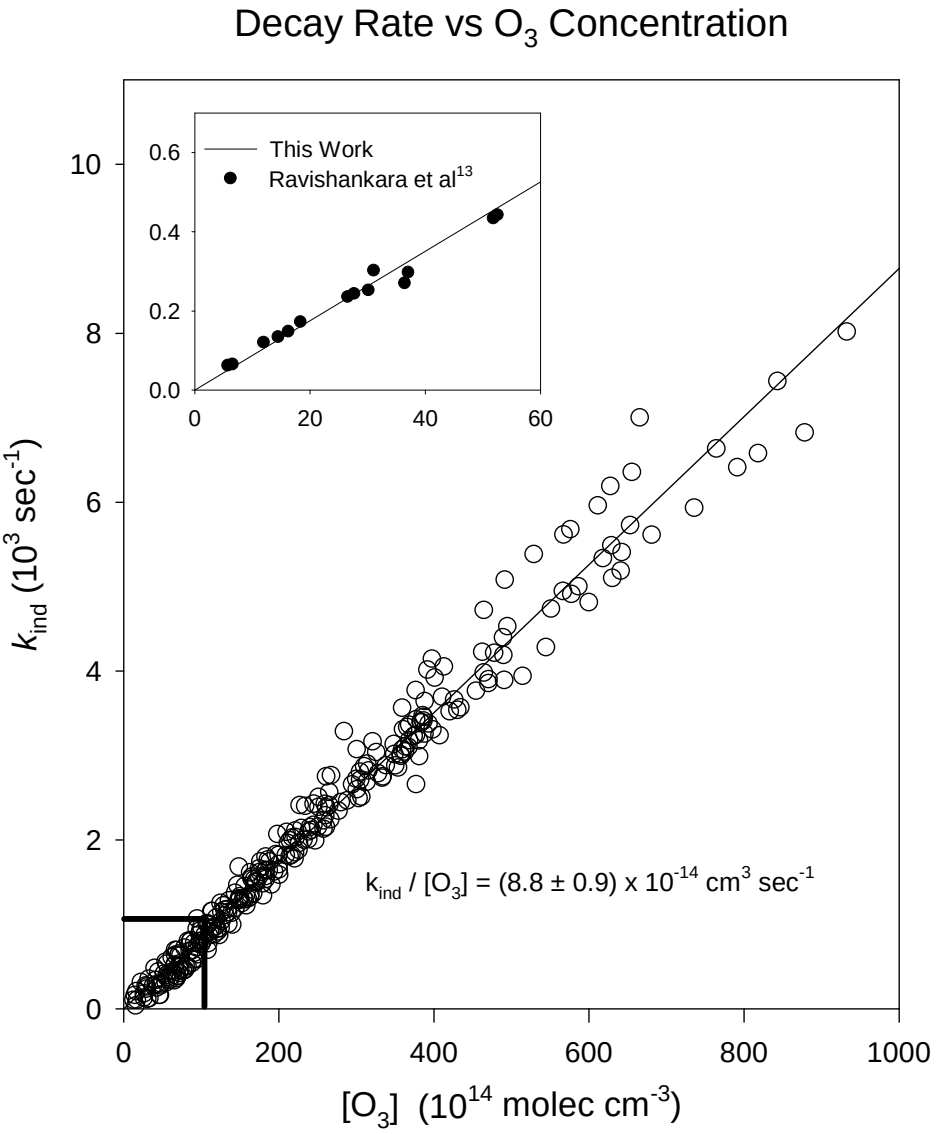

Figure 3-3. Stern-Volmer analysis of decay time vs ozone concentration at 298 K for various different experimental conditions. The slope represents the sum of the two chain rate constants, $k_{ind} = k_1 + k_2 = 8.8(90) \times 10^{-14}$ cm^3 $molecule^{-1}$ sec^{-1}. This data reflects ≈200 different sets of independent experimental conditions taken over several months, covering (i) a 10-fold range of excimer laser intensities (0.5 – 7.5 mJ/cm^2), (ii) 3-fold range of total cell pressure (16.7 – 45.0 Torr), and (iii) a 100-fold range of [O_3] (9.7 x 10^{14} and 9.5 x 10^{16} $molecules/cm^3$).

From the previous section, it is clear that this is not rigorously correct; for the $OH/HO_2/O_3$ chain reaction system, however, the magnitude of k_2 is thought to be only <5% of k_1, which explains why the second decay component would only be evident at high S/N in the previous studies. In the current studies, this double-exponential behavior is evident in all kinetic traces and is explicitly included in the kinetic analyses. Thus for consistency, the present results for k_{ind} should be compared with the earlier values reported for k_1 from previous studies that presumed a purely single-exponential decay.

These results are in agreement with the previous room temperature RF studies of Ravishankara et al.,[13] who report a rate constant of 8.2×10^{-14} cm^3 $molecule^{-1}$ s^{-1} . To make this more explicit, we have replotted the Ravishankara et al. data[13] on top of the current data (see inset region in Figure 3-3), which indicates a nearly quantitative overlap but also under-scores the ≈10-20 fold larger range of ozone concentrations that have been investigated via the IR laser absorption method.

Researcher	k_{ind}[298K] ($\times 10^{-14}$ cm^3/sec)
Anderson[11]	5.5 ± 1.5
Kurylo[12]	6.5 ± 0.5
Ravishankara[13]	8.2 ± 0.4
Smith[23]	7.5 ± 0.2
Recommended Value[14]	6.8
This work	8.8 ± 0.90

Table 3-3. Room temperature rate constants for k_{ind}.

As indicated in table 3-3, there is a relatively broad range of rate values reported in the literature[11-13,23]; our data is most consistent with the Ravishankara et al. value[13], verified over a much larger dynamic range of $[O_3]$. Of particular

importance, the presently determined value for k_{ind} is >20% higher than obtained from the k_1 and k_2 values recommended for use in atmospheric modeling.[14]

3.3 Systematic Checks

As additional confirmation of these results, the measurements have been repeated under a variety of diagnostic test conditions. The first is to assess for any effects due to nonlinear radical-radical kinetics, which one can systematically check by varying the laser power. The lack of any dependence on excimer laser power is displayed in figure 3-4, which indicate no change in the reported value of k_{ind} over a factor of 50 in laser pulse energy.

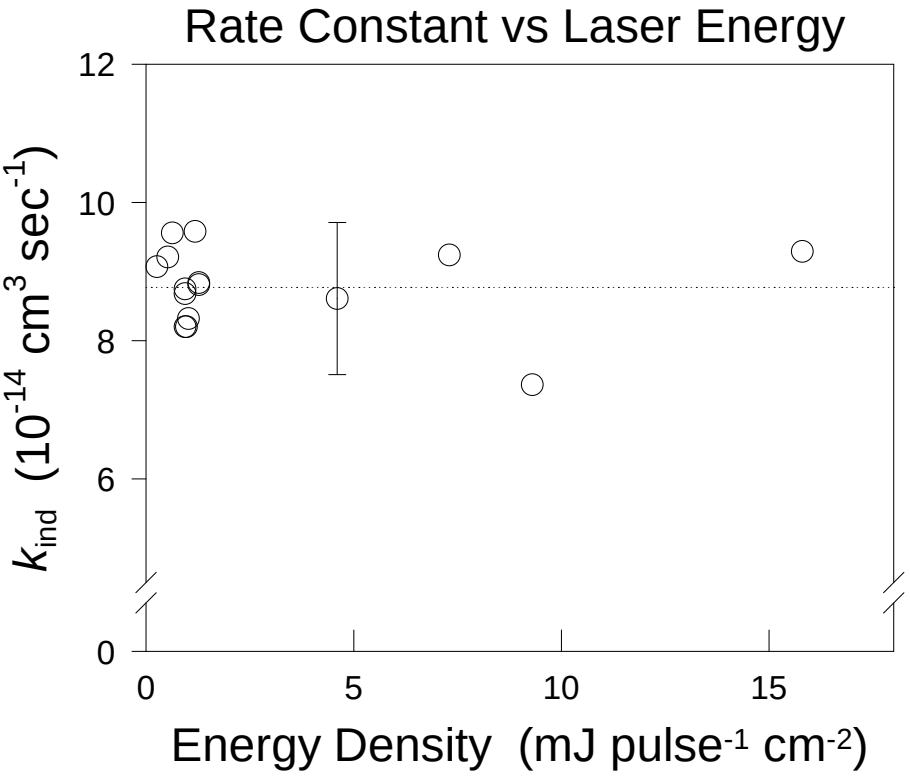

Figure 3-4. Room temperature rate constant as a function of excimer energy.

For comparison, most of the experiments reported in figure 3-3 are conducted with laser energy of <1 mJ/ cm^2 at a typical ozone concentration of 10^{16} molecules/cm^3 . This corresponds to an initial OH radical concentration of ≈1 x 10^{12} molecules/cm^3 and a $[OH]_0/[O_3]$ ratio of ≈1 x 10^{-4} . This low ratio of radical to O_3 concentrations ensures first-order kinetics and discriminates against contributions from even gas kinetic radical-radical reactions such as OH + HO_2 on the time scale of chain reaction induction period.

A second issue to address is the degree of thermal equilibration of the OH radical. As noted by Ravishankara et al.,[13] this can be particularly important in the $OH/HO_2/O_3$ chain reaction system due to acceleration of the OH + O_3 chain step by OH vibrational excitation[24]. To eliminate these interferences, the flow cell mixture contains high concentrations of H_2O, which is an extremely efficient quencher of vibrationally as well as rotationally excited OH radical. This can be tested in several ways. First of all, this degree of internal state relaxation is confirmed in figure 3-1, which indicates the excellent temporal separation between fast OH rovibrational relaxation and the much slower removal of OH by chain reaction with O_3. Secondly, since the IR probe laser is quantum state specific, we can monitor the chain kinetics on different rotational levels, which indicate no difference within experimental uncertainty. Furthermore, these kinetic measurements have been repeated for a variety of buffer gases (Ar, SF_6, N_2 and O_2) and cell pressures. As displayed in figure 3-5 the observed rates are remarkably insensitive to buffer gas conditions over the full range of data represented in figure 3-3.

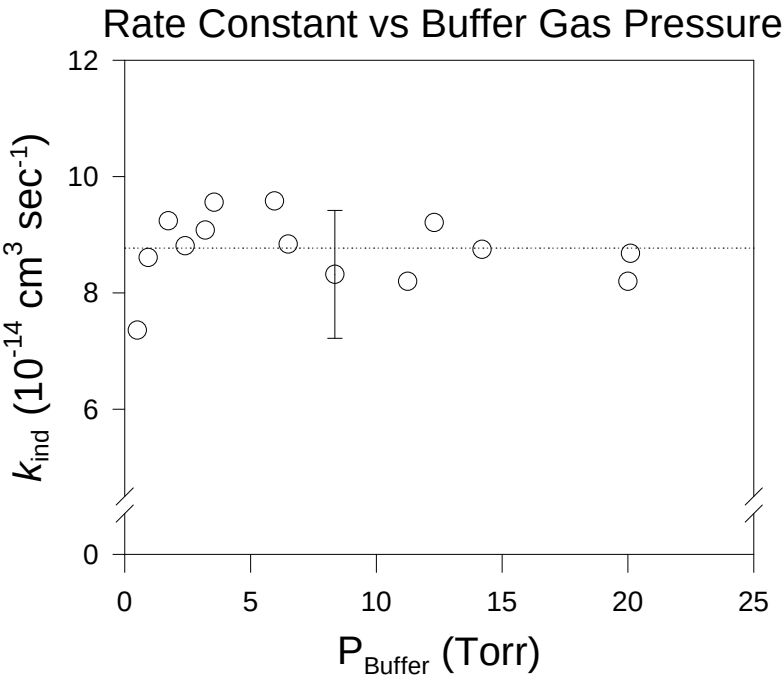

Figure 3-5. Room temperature rate constant as a function of buffer gas pressure.

3.4 Temperature Dependent Results

It is our goal to more fully understand the $OH/HO_2/O_3$ kinetics, especially at atmospheric temperatures. The region of the atmosphere where this chain reaction is most important has an average temperature of approximately 200 K. For this reason, it is important to the scientific community to have reliable kinetic data at these temperatures. Using our flash kinetic laser apparatus, in conjunction with the temperature controlled flow cell, we are able to observe the $OH/HO_2/O_3$ kinetics at various temperatures. Figure 3-7 presents the Stern-Volmer analysis for selected temperatures, while table 3-4 contains the experimental conditions and k_{ind} for these measurements.

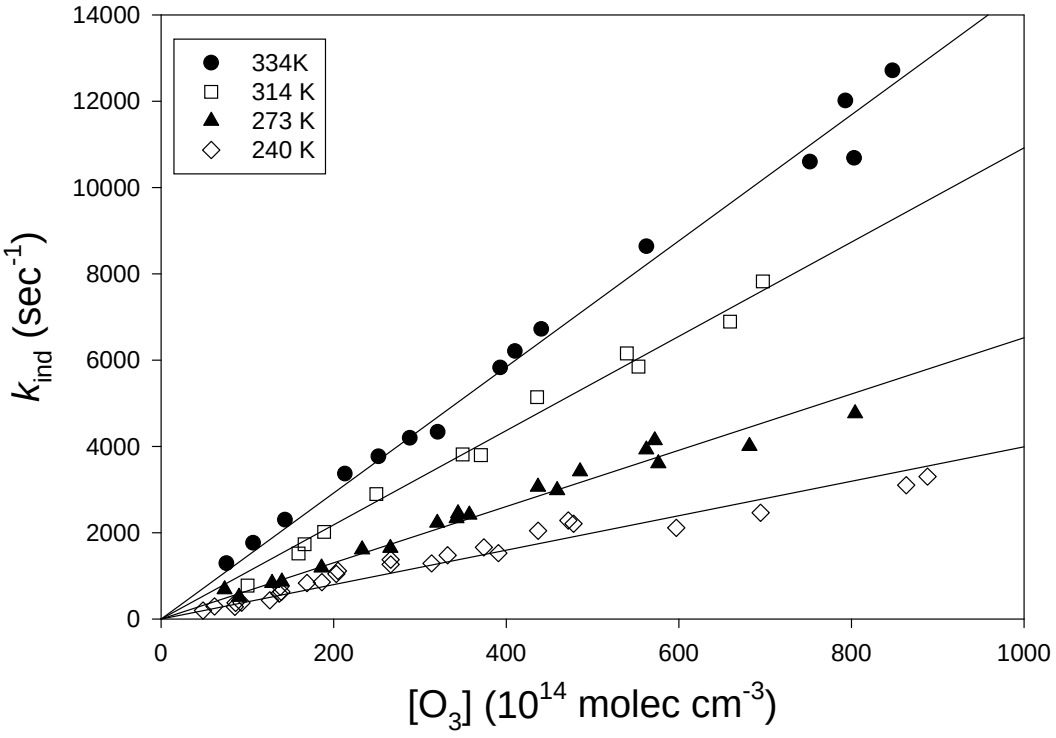

Figure 3-6. Stern-Volmer analysis of the decay time (k_{ind}) vs ozone concentration at four temperatures: 334 K, 314 K, 273 K, and 240 K.

Temp. (K)	P[H_2O] (Torr)	P[H_2] (Torr)	Total P (Torr)	k_{ind} (x 10^{-14} cm^3/sec)
334(2)	4.3	0	25	14.6(14)
314(1)	4.3	0	22	10.9(11)
295(2)	0.6 – 12.0	0 – 6	16 – 42	8.94(90)
287(1)	2.5	10	22	8.28(83)
273(1)	2.5	10	22	6.52(65)
266(2)	0.3	1.0 – 1.5	20 – 25	6.20(62)
253(1)	0.3	1.0 – 1.5	25	5.16(52)
250(2)	0.3	1 – 6	25	4.60(46)
240(2)	0.3	1 – 6	23	3.99(40)

Table 3-4. Typical conditions and k_{ind} at various temperatures.

In order to determine the temperature-dependence of the rate constant for the OH/O_3 chain reaction, an Arrhenius expression is utilized. The Arrhenius form for a temperature dependant rate constant is as follows:

$$k(T) = Ae^{-E_{Act}/T}, \tag{3.21}$$

where A is the Arrhenius pre-exponential factor, and E_{Act} is the Arrhenius activation energy for the reaction. Using this analysis, it is common to plot the rate constant, *k*, as a function of 1/T on a semi-log graph. If the reaction conforms to the Arrhenius expression, this will yield a straight line with a slope corresponding to the Arrhenius activation energy and an intercept corresponding to the pre-exponential factor. The result of this analysis is shown in figure 3-8, with the following Arrhenius parameters:

$$k_{\text{ind}}(T)\ \left[\frac{\text{cm}^3}{\text{sec}}\right] = \left(2.93^{+0.42}_{-0.38}\right) \times 10^{-12}\ \ \exp\left(\frac{-(1030 \pm 50)\text{K}}{T(\text{K})}\right). \tag{3.22}$$

Previous studies concerning the $OH/O_3/HO_2$ chain reaction have been reported in the literature. For purposes of comparison, we have included these previously determined rate constants in figure 3-8. It is apparent that agreement is within experimental error at low temperatures. However, at temperatures above 300 K, our values are consistently greater than those reported. Although the Arrhenius fit is quite good in this temperature window, our Arrhenius parameters are higher than those previously determined.

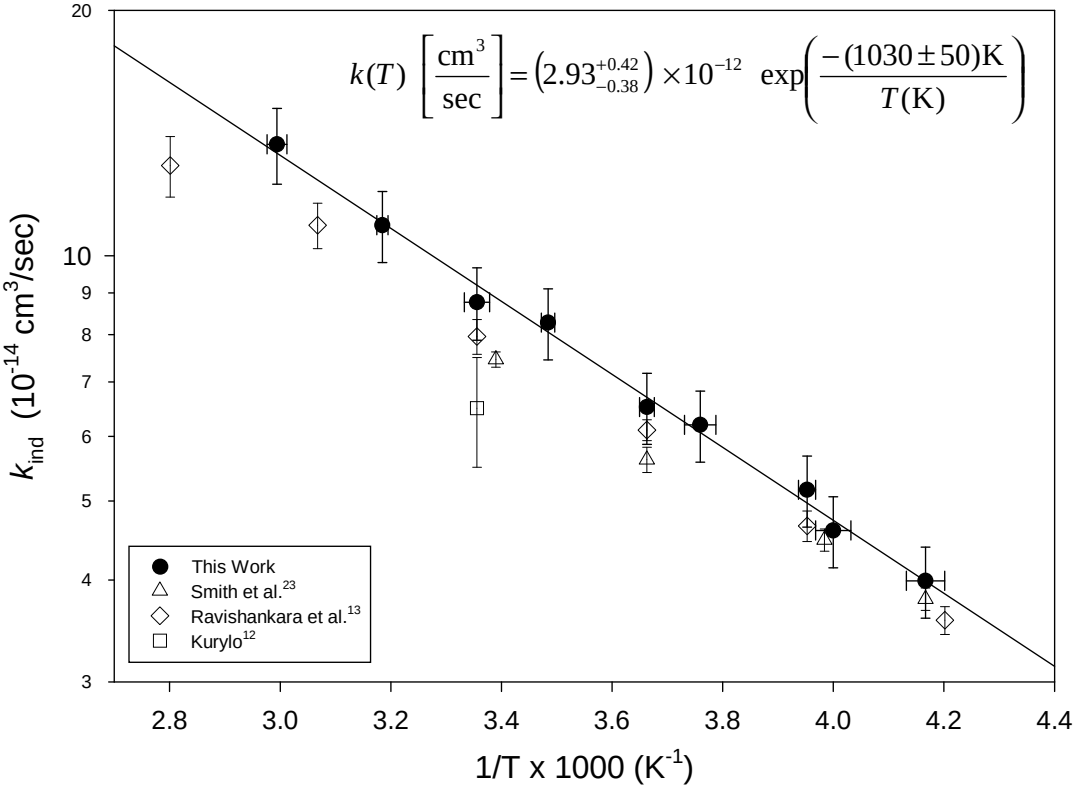

Figure 3-7. Arrhenius Plot for the induction decay rate, k_{ind}. Circles (•) represent our data, triangles (△) are from Smith et al.[23], diamonds (◊) are from Ravishankara et al.[13], and squares(□) are from Kurylo[12].

Researcher	k_{ind}[298K] (x 10^{-14} cm^3/sec)	A-Factor (cm^3/sec)	E/R (K)
Anderson[11]	5.5 ± 1.5	1.3 x 10^{-12}	960
Kurylo[12]	6.5 ± 0.5	--	--
Ravishankara[13]	8.2 ± 0.4	(1.82 ± 0.30) x 10^{-12}	930 ± 50
Smith[23]	7.5 ± 0.2	(1.52 ± 0.10) x 10^{-12}	890 ± 60
Recommended Value[14]	6.8	1.6 x 10^{-12}	940 ± 300
This work	8.8 ± 0.90	(2.93 ± 0.40) x 10^{-12}	1030 ± 50

Table 3-5. Comparison of k_{ind} with previously determined values.

It is worth speculating what these differences might be due to. The quantity most crucial to these rate constant determinations is the ozone number density. In an effort to minimize systematic errors, we use an *in situ* measurement of ozone density by absorption of the 308 nm photolysis light. However, the accuracy of this measurement is limited to the accuracy of the known cross section and its temperature dependence. In addition, when determining the Arrhenius parameters of the reaction, the values are quite sensitive to the temperature of the reactants. Obviously, any systematic errors in temperature measurement would lead to a discrepancy. In this study, the temperature of the gas was measured directly in two places in the cell: the middle and the far end. The agreement between these measurements are within 0.5^{o} C. In addition, we monitored the temperature of the circulating fluid, which would consistently be ~2^{o} C colder than the gas temperature during low temperature data runs and ~1^{o} C higher than the gas temperature during high temperature data runs. The thermocouples used in this investigation were calibrated with a mercury thermometer between 0 and 100^{o} C and found to be accurate to 0.5%.

3.5 k_2/k_{ind} Determination at Room Temperature

The determination of k_2 has proven to be more difficult. As presented above, the information needed to calculate k_2 is contained in the long-time tail of the OH decay curve. By comparing equation (3.21) with equation (3.18), one finds that the ratio of the back extrapolated intensities is equal to k_2/k_{ind}. Hence, in order to extract both k_1 and k_2, one must measure both the decay rate *and* the intensity

information. Unfortunately, intensity information is the most prone to systematic and experimental errors. In order to reduce these errors, a series of measurements were taken where special attention was paid to the determination of the ratio of k_2/k_{ind}. The result of these measurements (shown in figure 3-4) is k_2/k_{ind} = 0.043(2). These measurements were taken at 295K only, and we are currently working to extend these measurements to lower temperatures.

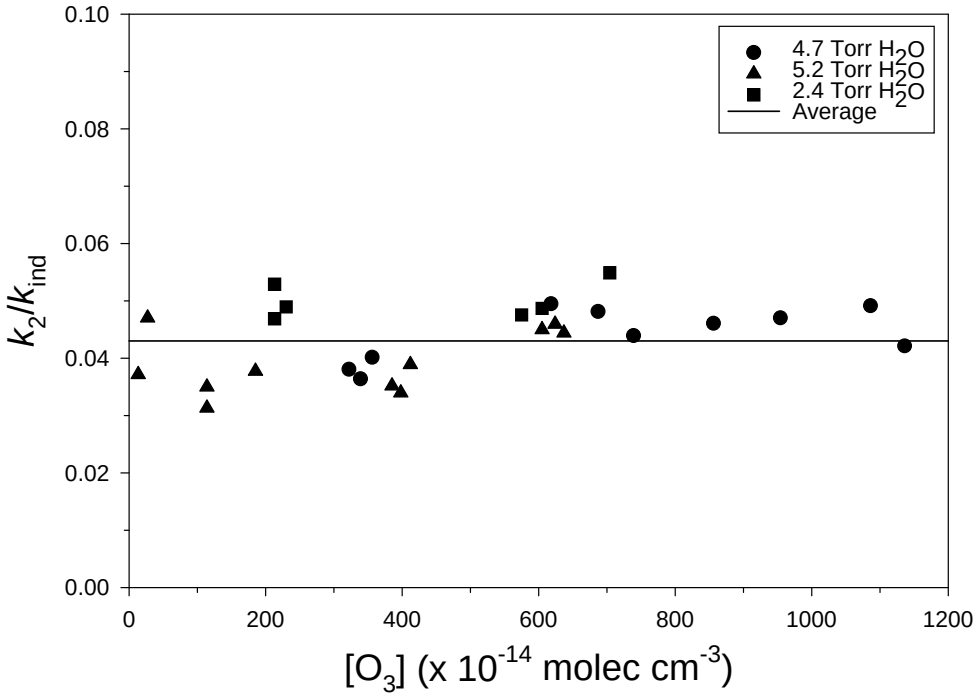

Figure 3-8. k_2/k_{ind} measurement at 295K. From this analysis, we calculate an average value to be 0.043(2).

This value can be compared with other, previous measurements of k_1 and k_2. Sinha et al.[22] report a k_2/k_1 value of 0.026(3) , which is consistent with the value of 0.029(3) value of Zahniser and Howard[25]. As presented in the previous sections, it

is appropriate to compare our k_2/k_{ind} to the previously measured values of k_2/k_1. Our value, however, is roughly 60% higher than these previous measurements. An explanation for this discrepancy is currently being pursued in our laboratory.

3.6 Breaking the 240 K Barrier

Extending the kinetic measurements below 240 K is not an easy task. At temperatures below 240 K, the vapor pressure of water becomes negligible, and the only source for OH atoms is through the reaction of $O(^1D)$ with H_2.

$$O(^1D) + H_2 \rightarrow OH + H \qquad (3.23)$$

This reaction proceeds at a gas-kinetic rate[14] (1.0×10^{-10} cm^3/sec) to form OH (v=0). However, the product H atom can react with ozone in the cell to form vibrationally excited OH[4,7].

$$H + O_3 \rightarrow OH(v \leq 9) + O_2 \qquad (3.24)$$

The branching ratio of the above reaction has been studied by Charters et al.[4], and more recently by Ohoyama et al.[6]. Ohoyama et al. has shown that 80% of the nascent vibrational distribution of OH is in $v \geq 7$. Without H_2O present in the cell to rapidly quench the vibrationally excited OH into its ground state, its presence serves to severely complicate the kinetics. First of all, the rate of $OH(v \geq 7)$ and O_3 is two orders of magnitude faster[21] than the rate of ground state OH. In addition, the collisional relaxation of $OH(v \geq 1)$ by the Ar buffer gas will lengthen the initial OH rise time by two orders of magnitude. A plot of sample data where H_2 is the only precursor is shown in figure 3-10. One will notice the initial *emission* signal at time t = 0, signifying a population inversion with respect to the upper state, namely OH

(v=1, J= 1.5). This emission signal is followed by an extremely slow rise (t ~ 0.5 msec), which eventually turns around to form an exponential decay. This decay terminates to a greatly exaggerated offset, a consequence of the quickly generated HO_2 product from OH(v≥9) and O_3.

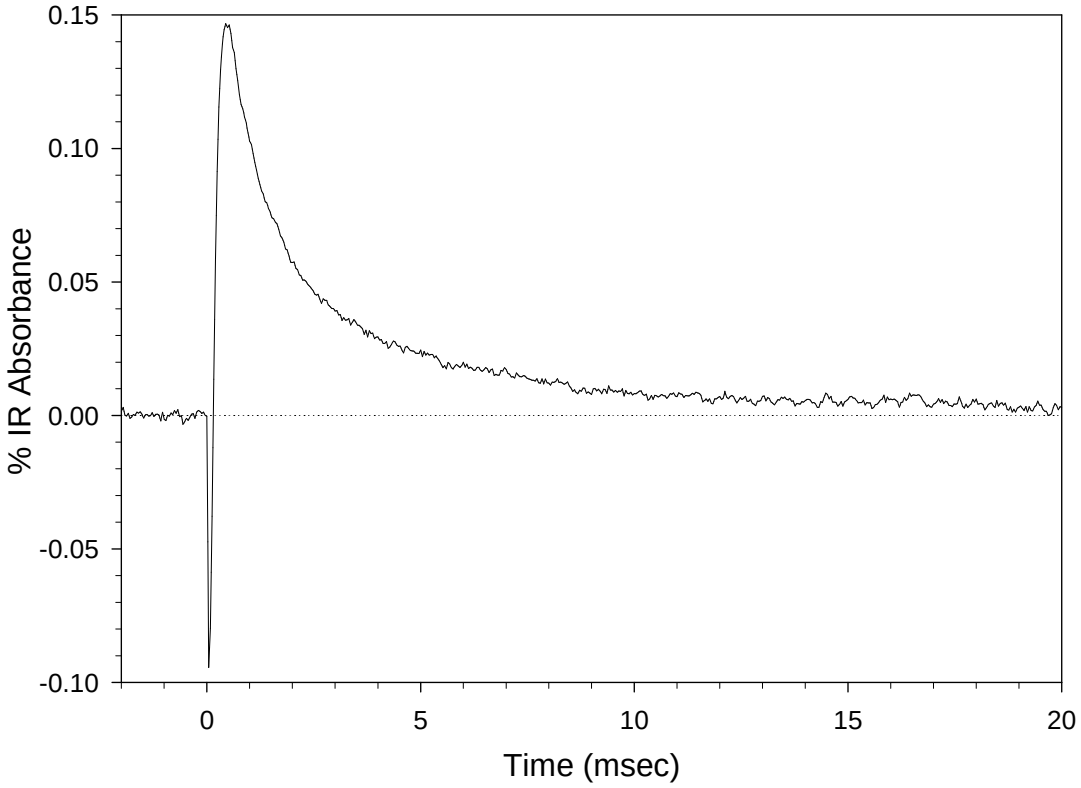

Figure 3-9. Typical OH absorption data when H_2 is used as the sole precursor. This data is taken on the OH v=0, P(2.5)1⁻ transition. Notice the initial emission signal, indicating an initial population inversion. The slow rise time is indicative of the decreased timescale for vibrational and rotational relaxation. The conditions for this data is as follows: $[H_2]$ = 12.0 Torr, $[O_3]$ = 0.30 Torr, [Ar] = 17 Torr, XeCl laser energy = 0.5 mJ/pulse.

However, it is still possible to extract the initial exponential decay and observe how the induction rate, kind, varies with respect to ozone concentration in the flow cell. The results of this analysis is shown in figure 3-11.

Temp. (K)	P[H_2O] (Torr)	P[H_2] (Torr)	Total P (Torr)	k_{ind} (x 10^{-14} cm^3/sec)
230(2)	0	13	30	2.38(48)
220(2)	0	12	28	2.02(40)
210(2)	0	13	30	1.44(29)
200(2)	0	12	29	0.77(15)

Table 3-6. Experimental conditions and results of OH + O_3 kinetic data taken below 240 K using H_2 as the sole precursor.

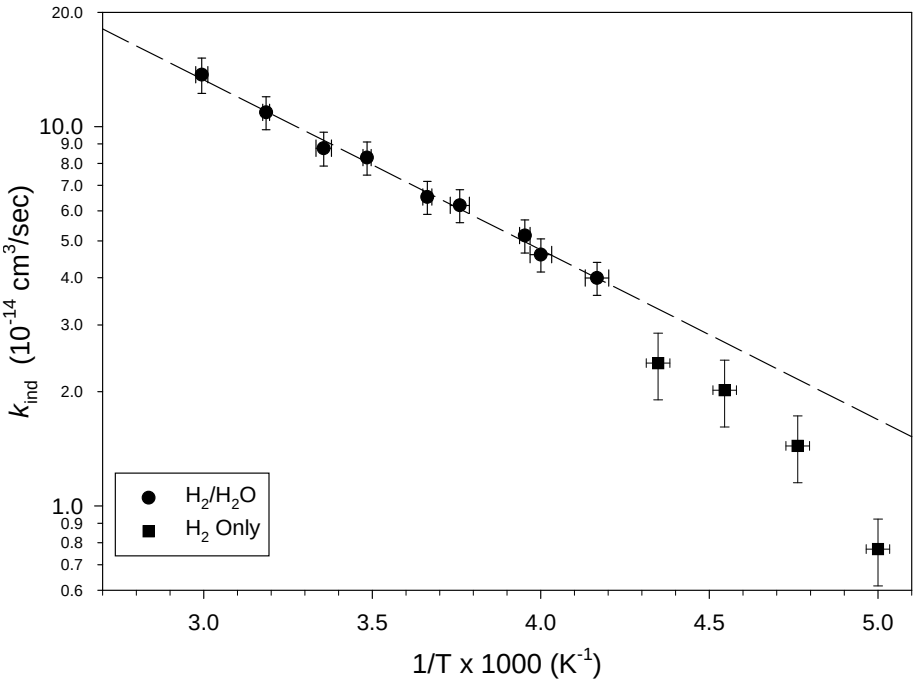

Figure 3-10. Arrhenius plot comparing data with and without H_2O present in the flow cell. The decrease in rate constant when H_2 is used as the sole precursor is obvious in the data. A possible explanation for this discrepancy is a reaction involving H_2 and vibrationally excited OH.

It is obvious that a sharp break occurs in the Arrhenius plot at temperatures below 240 K. It is important to investigate possible explanations for these values

and determine how much, if at all, the rate constant, k_{ind}, is changed when H_2 is the only precursor present in the cell. Ravishankara et al.[13] report a decrease in the reaction rate when H_2 is the only precursor is present, which is consistent with the observations made in this study. Ravishankara et al. attribute the slower decay rate to a chain reaction involving vibrationally excited OH and H_2, which re-forms vibrationally excited OH:

$$OH\ (v\geq 1) + H_2 \rightarrow H_2O + H \qquad (3.25)$$

$$H + O_3 \rightarrow OH(v\leq 9) + O_2 \qquad (3.26)$$

The above reaction scheme is only active when the time scale for OH ($v\geq 1$) reacting with H_2 is less than the time scale for OH($v\geq 1$) relaxation into OH($v=0$). Spencer et al.[26] have studied reaction (3.25) and concluded that the rate constant for the reaction of OH($v=1,2$) + H_2 is $<1 \times 10^{-14}$ cm^3/sec, while the rate constants for relaxation of OH($v=1,2$) are $\approx 1 \times 10^{-14}$ cm^3/sec (see table 3.1). When we consider the high concentrations of H_2 in the cell, which dictate the time scale for the OH($v\geq 1$) + H_2 reaction, it very possible that this chain will play a role in complicating the OH + O_3 kinetics. In order for this chain to be negligible under the conditions of this experiment, the rate of reaction 3.25 must be $<1 \times 10^{-15}$ cm^3/sec. Therefore, if the rate constant of reaction 3.25 is between 1×10^{-15} and 1×10^{-14} cm^3/sec, then we would expect complications due to the chain reaction presented above.

3.7 Conclusion

The primary thrust of this work has been to determine the temperature dependant rate constant of ozone depleting chain reaction involving OH and HO_2,

by utilizing direct infrared absorption. A pseudo first order kinetic analysis is presented which correctly predicts the OH time dependence to be double exponential, with an initial exponential component determined by the sum of the two chain rate constants (i.e. $k_{ind} = k_1 + k_2$). Furthermore, this chain "induction" feature decays to a nonzero OH concentration in the steady-state chain propagation regime, which is also confirmed by experimental results. This analysis differs from the previous LIF/RF studies of $OH + O_3$, which neglect chain effects due to the $HO_2 + O_3$ reaction and treat the loss of OH as a single exponential decay to zero determined only by k_1. Our data analysis yields a value for k_{ind} which is confirmed over a much higher dynamic range of ozone concentrations than previously accessible by LIF and RF methods.

References for Chapter 3

1 P. H. Wine and A. R. Ravishankara, *Chem. Phys.* **69,** 365 (1982).

2 J. E. Butler, L. D. Talley, G. K. Smith, and M. C. Lin, *J. Chem. Phys.* **74,** 4501 (1981).

3 J. A. Davidson, H. I. Schiff, T. J. Brown, and C. J. Howard, *J. Chem. Phys.* **69,** 4277 (1978).

4 P. E. Charters, R. G. Macdonald, and J. C. Polanyi, *Appl. Opt.* **10,** 1747 (1971).

5 J. H. Lee, J. V. Michael, W. A. Payne, and L. J. Stief, *J. Chem. Phys.* **69,** 350 (1978).

6 H. Ohoyama, T. Kasai, Y. Yoshimura, H. Kimura, and K. Kuwata, *Chem. Phys. Lett.* **118,** 263 (1985).

7 B. J. Finlayson-Pitts and T. E. Kleindienst, *J. Chem. Phys.* **74,** 5643 (1981).

8 J. E. Davenport, B. Ridley, H. I. Schiff, and K. H. Welge, *J. Chem. Soc. Faraday Disc.* **53,** 230 (1972).

9 L. C. Lee and T. G. Slanger, *J. Chem. Phys.* **69,** 4053 (1978).

10 G. E. Streit, C. J. Howard, A. L. Schmeltekopf, J. A. Davidson, and H. I. Schiff, *J. Chem. Phys.* **65,** 4761 (1976).

11 J. G. Anderson and F. Kaufman, *Chem. Phys. Lett.* **19,** 483 (1973).

12 M. J. Kurylo, *Chem. Phys. Lett.* **23,** 467 (1973).

13 A. R. Ravishankara, P. H. Wine, and A. O. Langford, *J. Chem. Phys.* **70,** 984 (1979).

14 W. B. DeMore, S. P. Sander, D. M. Golden, R. F. Hampson, M. J. Kurylo, C. J. Howard, A. R. Ravishankara, C. E. Kolb, and M. J. Molina, (Jet Propulsion Laboratory, Pasedena, 1994).

15 G. P. Glass, H. Endo, and B. K. Chaturvedi, *J. Chem. Phys.* **77,** 5450 (1982).

16 G. C. Light and J. H. Matsumoto, *Chem. Phys. Lett.* **58,** 578 (1978).

17 J. A. Dodd, S. J. Lipson, and W. A. M. Blumberg, *J. Chem. Phys.* **95,** 5752 (1991).

18 K. J. Rensberger, J. B. Jeffries, and D. R. Crosley, *J. Chem. Phys.* **90,** 2174 (1989).

19 K. N. Rensberger, J. B. Jeffries, and D. R. Crosley, *J. Chem. Phys.* **90,** 2174 (1988).

20 A. E. Potter, R. N. Coltharp, and S. D. Worley, *J. Chem. Phys.* **54,** 992 (1970).

21 R. N. Coltharp, S. D. Worley, and A. E. Potter, *Appl. Opt.* **10,** 1786 (1971).

22 A. Sinha, E. R. Lovejoy, and C. J. Howard, *J. Chem. Phys.* **87,** 2122 (1987).

23 C. A. Smith, L. T. Molina, J. J. Lamb, and M. J. Molina, *Int. J. Chem. Kin.* **16,** 42 (1984).

24 G. E. Streit and H. S. Johnston, *J. Chem. Phys.* **64,** 95 (1976).

25 M. S. Zahniser and C. J. Howard, *J. Chem. Phys.* **73,** 1620 (1980).

26 J. E. Spencer, H. Endo, and G. P. Glass, *16th (International) Sympolium on Combustion* **,** 829 (1976).

CHAPTER 4

$F + H_2$ REACTIVE SCATTERING

4.1 Introduction

Ever since the pioneering work of Polanyi and co-workers on atom + diatom reactive collision dynamics,[1-3] there has been an intense interest in reactive scattering on $F + H_2 \rightarrow HF(v, J) + H$ from the chemical physics community.[4] The reasons for strong theoretical interest in this fundamental chemical reaction are readily appreciated. First of all, the $F + H_2$ system is an excellent prototype of a low barrier exothermic chemical reaction, yet small enough in total electron number and nuclear degrees of freedom to be tractable via high level *ab initio* calculations. This has led to the development of several potential energy surfaces,[5-10] which has facilitated detailed classical,[11,12] and quasi-classical[13-15] studies of the $F + H_2$ reaction dynamics, as well as prediction of electron energy distributions from $[FH_2]^-$ photo detachment studies.[16,17] Most importantly, there have been breakthroughs in three atom quantum reactive scattering that make feasible a numerically *exact* treatment of the reaction dynamics for a given adiabatic potential surface.[17-21] As a

result, F + H_2 has evolved to become the "benchmark" chemical reaction system with which to compare experiment against theory at a fully rigorous level.

This theoretical interest has been stimulated by corresponding experimental efforts. Arrested relaxation methods of Polanyi and co-workers were first used to probe the HF(v, *J*) rotational distributions via low pressure FTIR chemiluminescence methods.[1] Due to long residence times in the FTIR detection region, however, substantial collisional redistribution of the nascent HF product could occur; thus, "nascent" rovibrational distributions were estimated by extrapolation to the zero pressure limit. Crossed molecular beam methods by both Lee and co-workers at Berkeley[22-24] and Toennies and co-workers at Goettingen[25-27] have been used to investigate the *differential* reactive scattering of F + H_2 and isotropic variants for a series of center-of-mass collision energies. Due to limited energy resolution in these time-of-flight studies, however, only vibrational product levels could be resolved, with limited information on HF rotational distributions inferred from contour analysis. There has recently been a report from the Keil group of a measurement based on HF chemical laser excitation and bolometric detection that provides angularly resolved reactive scattering information on a single HF product quantum state.[28]

The thrust of this chapter is to report a new IR laser based method for obtaining nascent product state distributions from F + H_2 under single collision conditions. Our approach is based on the following combination: i) A pulsed supersonic discharge source of F atoms is collided with a second pulsed jet source of H_2 molecules under sufficiently low densities to ensure single collision,

molecular beam conditions; ii) the product HF(v, *J*) is probed in the intersection region by high sensitivity direct absorption of a single mode tunable IR laser; and iii) as a function of laser tuning, these spectral data yield Doppler limited absorbance profiles on reactively scattered product HF(v, *J*)with complete resolution of final vibration/rotation quantum state. A complete description of the experimental method and results will be presented elsewhere;[29] this communication focuses on the highest vibrational manifold [i.e., HF(v=3, *J*)] that is energetically accessible at 1.8(2) kcal/mol center of mass collision energy, E_{com}.

Such results provide the first opportunity for a fully rigorous comparison with exact quantum theoretical predictions of reactive scattering by Castillo and Manolopoulos[21] on the lowest adiabatic F + H_2 potential energy surface of Stark and Werner.[10] The agreement is found to be reasonably good, but theory substantially under predicts the high *J* rotational distributions near the energetic upper limit. These data provide indications that nonadiabatic channels involving both ground F($^2P_{3/2}$) and spin orbit excited F*($^2P_{1/2}$) atoms may be participating in the reaction dynamics.

4.2 Experiment

The experimental apparatus for state-to-state *reactive* scattering of F + H_2 is based on a modification of our earlier apparatus for state-to-state *inelastic* scattering, and is depicted schematically in figure 4-1. A pulsed discharge is used to generate high densities of F atoms upstream of the limiting expansion orifice (800 μm diameter) of an axisymmetric super-sonic jet. The stagnation gas is 5% F_2 in He obtained from a commercial excimer laser gas premix. The discharge is struck by

negatively biasing the orifice with respect to the valve body by ≈ 600 V, which results in 35 mA currents stabilized by a 5 kΩ ballast resistor in series with the discharge. Pulsed timing circuits are used to confine the discharge to a 200 μs window near the peak of the full gas pulse (800 μs). The H_2 supersonic jet is formed through a 200 μm diameter pinhole with a piezoelectric actuator based on the design of Proch and Trickl.[30]

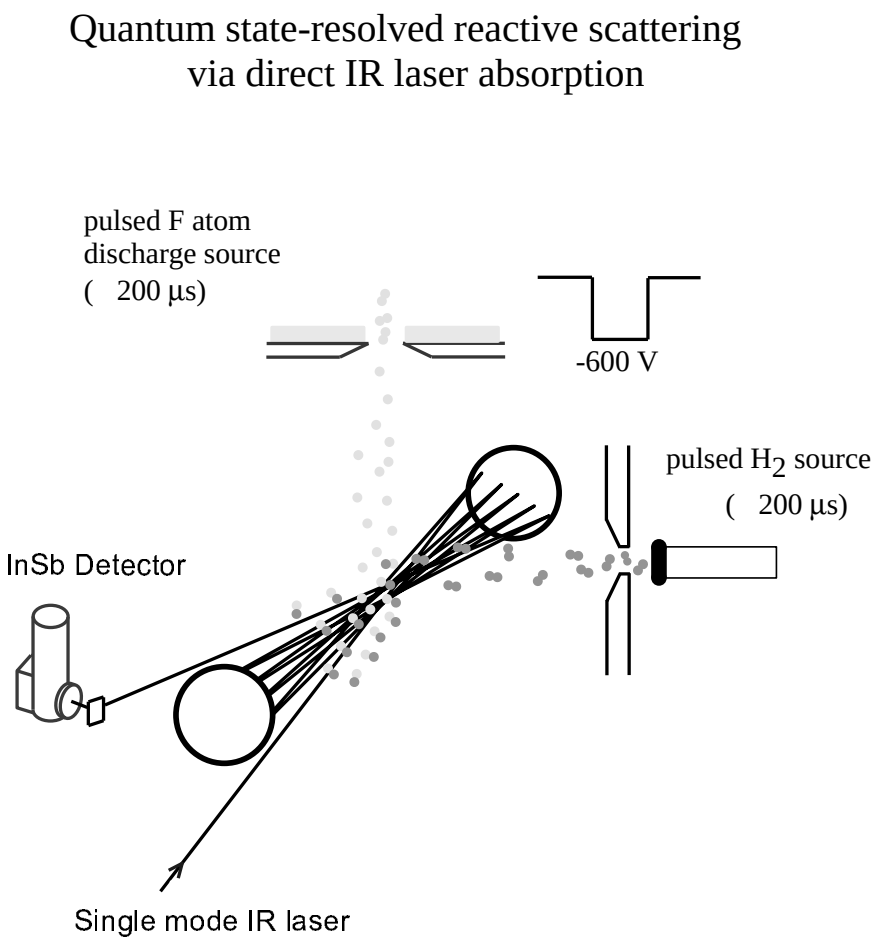

Figure 4-1. Schematic diagram of the crossed jet direct absorption reactive scattering experiment. Fluorine atoms produced in a discharge pulsed jet expansion are intersected at a 90° angle 4.5 cm downstream with a pulse of supersonically cooled H_2. Tunable single mode IR laser light is multi-passed perpendicular to the collision plane and probes HF(v, *J*) products by direct absorption.

The column integrated number density of H_2 in the intersection region is directly calibrated in a separate experiment by doping CH_4 into the stagnation gases at ≈1% level, and then monitoring direct IR absorption on the ν_3 CH stretch absorption band. Boltzmann analysis of the CH_4 rotational distribution estimates the rotational temperature of the H_2 reagent to be <30 K. Even at 100 K, H_2 is cooled essentially completely down into its lowest nuclear spin allowed states, namely j=1 (ortho) and j=0 (para) in a 3:1 ratio, with the first excited para (j =2) and ortho (j =3) states down 100- to 1000-fold.

The jets intersect 4.5 cm downstream of the nozzles, where for a typical 200 Torr H_2 backing pressure, the F atoms have a reaction probability of only ≈2%. Thus the probability of secondary inelastic collisions of the reaction products can be neglected, as explicitly verified by H_2 stagnation pressure studies. The temporal evolution of both gas pulses is monitored with miniature hearing aid microphones mounted inside the vacuum chamber on translational stages; time delay studies of the gas pulses are used to measure the velocity distributions for each beam. The H_2 and F atom beam velocities are 2.47(13) x 10^5 cm/s and 1.45(7) x 10^5 cm/s, respectively, which for the right angle collision geometry translates into E_{com} =1.8(2) kcal/mol. The 0.2 kcal/mol uncertainty arises predominantly from the finite spread in collision angles and is experimentally determined from Doppler profiles and Monte Carlo modeling. This energy width is more than threefold smaller than the rotational energy spacing between J = 4 and 5, and thus has a negligible effect on the product state distributions. The center-of-mass collision energy is essentially

equal to the 1.84 kcal/mol value used in previous quantum calculations of Castillo and Manolopoulos, which forms the basis of all comparison with theory in this chapter. The HF(v, J) reaction products are probed by direct absorption of a single mode color center laser that is multi-passed 16 times through the intersection region in a cylindrical Herriot cell.[31] Absorption measurements are performed on the $\Delta v = +1$ fundamental HF band, and measure population *differences* between the upper and lower levels. Shot-noise limited absorption sensitivity is achieved by a combination of i) dual beam differential detection on matched InSb detectors and ii) electro-optic servo loop control of the color center laser intensity. All HF product signals are monitored on $\Delta v = +1$ P or R branch transitions, the frequencies for which are well determined and measured with a traveling wave meter of the Hall and Lee design.[32] This yields readily detectable HF signals at 10^{-5} absorbance levels, which translate into sensitivities of $<1 \times 10^{8}$ /cm^{3} /quantum state.

4.3 Results and Analysis

For each rotationally resolved transition, the time resolved HF signals are captured by a transient digitizer, integrated over the pulse duration, and stored on computer as a function of laser detuning. Sample results for J-dependent absorption signals in the HF($v = 3$,J) manifold are shown in figure 4-2, demonstrating velocity resolved Doppler profiles for the nascent HF product. Since this is a coherent absorption measurement, the HF($v = 3$,J) signals rigorously reflect population *differences* between the upper and lower rovibrational states. However, HF ($v = 4$, J=0) is energetically inaccessible to both F and F* at E_{com} = 1.8(2) kcal/mol; thus the $v=4 \leftarrow 3$ signals in figure 4.2 reflect pure absorbance due solely to optical excitation

out of the HF(v = 3, *J*) manifold. These absolute absorbances are rigorously converted[33] to absolute population densities per unit velocity subgroup by the IR linestrengths experimentally measured by Setser and co-workers from chemiluminescence studies.[34] We restrict our focus in this paper on state resolved *integral* scattering cross sections obtained by integrating over all Doppler velocity components, this yields the absolute *column integrated* populations i.e., molecules/cm^2) for a given final *J* state over the region sampled by the probe laser beam.[33]

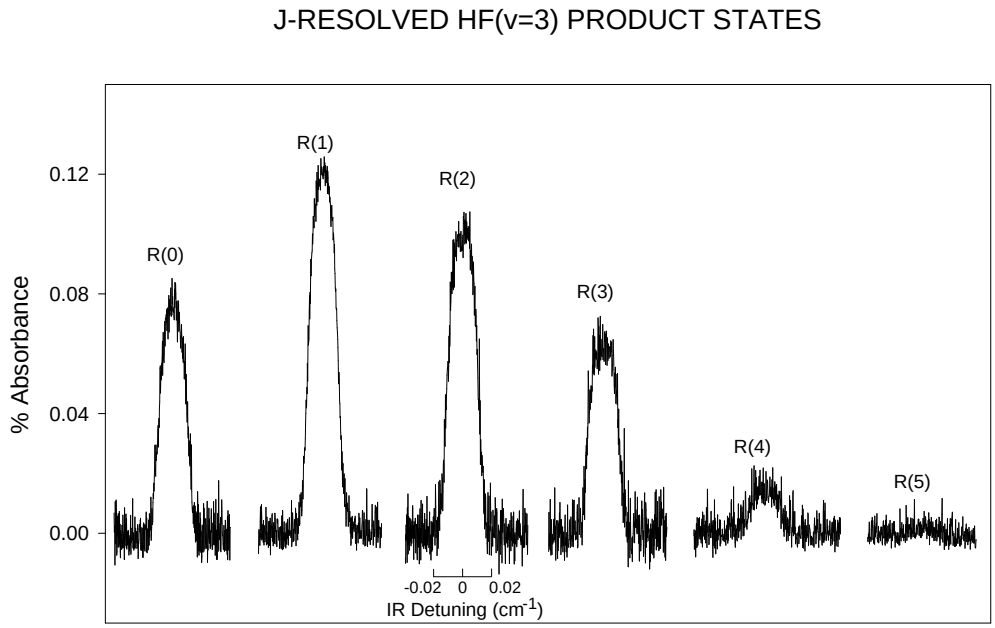

Figure 4-2. Sample absorption signals from HF(v=3) produced by reactive scattering of F atoms with H_2. Nascent population is evident in all *J* levels up to the energetic limit for the 1.8(2) kcal/mol center of mass collision energy.

4.4 Comparison with Theory

The highest level theoretical studies done to date on the F + H_2(*j*) system have been the quantum reactive scattering calculations performed by Castillo and Manolopoulos,[21] which predict differential and integral cross sections into given HF(v, *J*) states on the lowest adiabatic potential surface of Stark and Werner.[10] These differential cross sections can be related to the experimentally observed column integrated populations by center-of-mass to lab frame transformation. However, the resulting flux-to-concentration transformation between integral cross sections and populations for the current scattering geometry, kinematic mass combinations and energetics proves to be essentially independent of *J*. Thus to a very good approximation we can directly compare the experimental column integrated populations with the theoretical integral cross sections, averaged over the1:3 nuclear spin distribution of *j* =0 (para) and *j* =1 (ortho) H_2 in the jet. This comparison is shown in figure 4-3, where the column integrated populations have been scaled to the integral cross section into *J* = 1. Overall the agreement between experiment and theory is quite good, with general trends in the experimental data well reproduced by theory. Agreement for the lower *J* values is especially quantitative, capturing the rise from *J* = 0 to nearly equivalent populations experimentally seen in *J* = 1 and 2. Given that these results are based on fully *ab initio* calculations and exact quantum scattering codes, this level of agreement serves to confirm the reliability of the Stark and Werner potential surface for this "bench-mark" atom + diatom reaction system. However, there are also substantial discrepancies between these theoretical predictions and experiment at higher *J*

values. Specifically, theory systematically *under-predicts* the populations in $J > 3$, by factors that greatly exceed the experimental uncertainty of the measurements. Indeed, the $J = 3$ experimental values are nearly two-fold larger than theoretically predicted, while this factor grows to nearly six-fold for $J = 4$. This effect is most dramatic in $J = 5$, which is an energetically closed channel on the Stark and Werner surface i.e., the integral cross section vanishes, whereas experimental signals clearly exist out to $J = 5$. Note that this is not plausibly due to finite resolution, since the energy difference between $J = 4$ and 5 is more than three-fold greater than experimental width in E_{com}.

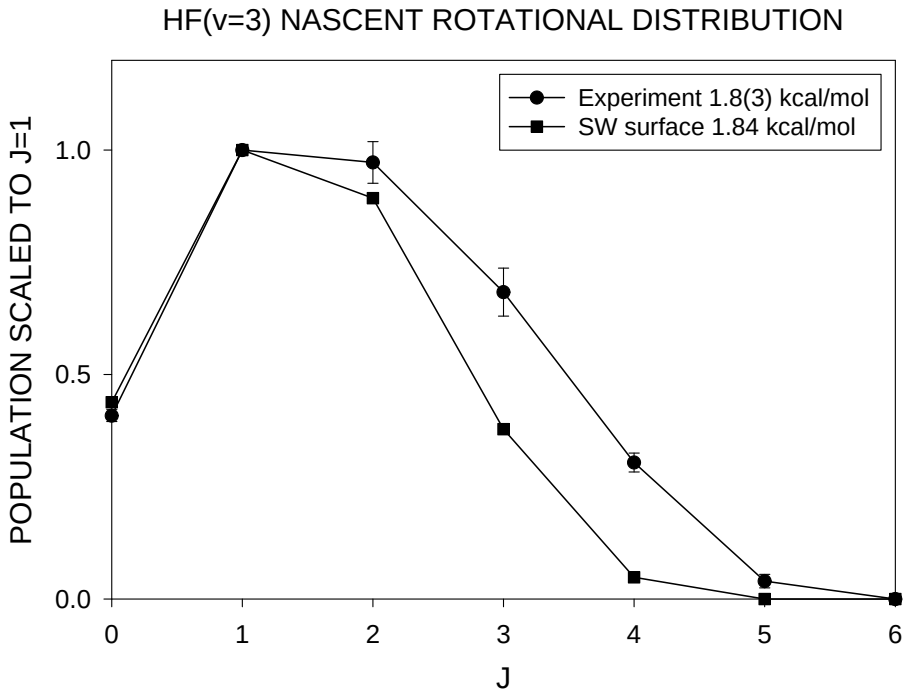

Figure 4-3. Nascent rotational distribution for F + H2 → HF(v = 3) + H at E_{com} = 1.8(2) kcal/mol (circles) compared to full quantum reactive scattering calculations (squares) by Castillo and Manolopoulos at 1.84 kcal/mol on the lowest adiabatic surface of Stark and Werner. Note the substantial underprediction of populations in $J \geq 3$.

As a final comment, it is worth speculating on what the high *J* discrepancies between experiment and theory might be due to. The quantum reactive scattering calculations of Castillo and Manolopoulos are "exact" for reactions on a given adiabatic potential surface; thus the simplest interpretation would be that these high *J* discrepancies may reflect deficiencies in Stark and Werner's lowest adiabatic surface in the barrier region. Alternatively, it is possible that the $F + H_2$ reactions do not take place exclusively on the single lowest *adiabatic* potential surface, though this has been explicitly assumed in all $F + H_2$ quantum reactive scattering calculations thus far. If *nonadiabatic* effects are important, then one would also anticipate contributions to reactive scattering from low lying spin orbit excited $F^*(^2P_{1/2})$ atoms also present in the jet. Given the 1.16 kcal/mol (404 cm^{-1}) spin orbit splitting between F and F^*, this would help explain the excess population experimentally observed in $J > 3$. The intriguing possibility of nonadiabatic $F^* + H_2$ reaction pathways can be tested experimentally by lowering the center-of-mass collision energy below the energetic threshold for forming a specific HF(v, *J*) product state from the purely adiabatic $F + H_2$ reaction channel. These and other threshold studies are currently being pursued in our laboratory.

References for Chapter 4

1 J. C. Polanyi and K. B. Woodall, *J. Chem. Phys.* **57,** 1574 (1972).

2 D. H. Maylotte, J. C. Polanyi, and K. B. Woodall, *J. Chem. Phys.* **57,** 1547 (1972).

3 F. E. Bartoszek, D. M. Manos, and J. C. Polanyi, *J. Chem. Phys.* **69,** 933 (1978).

4 D. E. Manolopoulos, *J. Chem. soc., Faraday Trans.* **93,** 673 (1997).

5 C. F. Bender, P. K. Pearson, S. V. ONeil, and H. F. Schaefer III, *J. Chem. Phys.* **56,** 4626 (1972).

6 J. T. Muckerman, *J. Chem. Phys.* **56,** 2997 (1972).

7 R. Steckler, D. G. Truhlar, and B. C. Garrett, *J. Chem. Phys.* **82,** 5499 (1985).

8 T. Takayanagi and S. Sato, *Chem. Phys. Lett.* **144,** 191 (1988).

9 G. C. Lynch, R. Steckler, D. W. Schwenke, A. J. C. Varandas, and D. G. Truhlar, *J. Chem. Phys.* **94,** 7136 (1991).

10 K. Stark and H.-J. Werner, *J. Chem. Phys.* **104,** 6515 (1996).

11 R. L. Jaffe, J. M. Henry, and J. B. Anderson, *J. Chem. Phys.* **59,** 1128 (1973).

12 J. T. Muckerman, *J. Chem. Phys.* **57,** 3382 (1972).

13 W. Jakubetz and J. N. L. Connor, *Faraday Discuss. Chem. Soc.* **62,** 324 (1977).

14 D. Neuhauser, R. S. Judson, R. L. Jaffe, M. Baer, and D. J. Kouri, *Chem. Phys. Lett.* **176,** 546 (1991).

15 F. J. Aoiz, L. Banares, V. J. Herrero, V. Saez Rabanos, K. Stark, and H.-J. Werner, *J. Chem. Phys.* **102,** 10665 (1994).

16 S. E. Bradforth, D. W. Arnold, D. M. Neumark, and D. E. Manolopouls, *J. Chem. Phys.* **99,** 6345 (1993).

17 D. E. Manolopoulos, K. Stark, H.-J. Werner, D. W. Arnold, S. E. Bradforth, and D. M. Neumark, *Science* **262** (1993).

18 J. Z. H. Zhang and W. H. Miller, *J. Chem. Phys.* **88,** 4549 (88).

19 J. M. Launay and M. Le Dourneuf, *Chem. Phys. Lett.* **169,** 473 (1990).

20 J. Z. H. Zhang, *Chem. Phys. Lett.* **181,** 63 (1991).

21 J. F. Castillo, D. E. Manolopoulous, K. Stark, and H.-J. Werner, *J. Chem. Phys.* **104,** 6531 (1996).

22 T. P. Schafer, P. E. Siska, J. M. Parson, F. P. Tully, Y. C. Wong, and Y. T. Lee, *J. Chem. Phys.* **53,** 3385 (1970).

23 D. M. Neumark, A. M. Wodtke, G. N. Robinson, C. C. Hayden, and Y. T. Lee, *J. Chem. Phys.* **82,** 3045 (1985).

24 D. M. Neumark, A. M. Wodtke, G. N. Robinson, C. C. Hayden, K. Shobatake, R. K. Sparks, T. P. Schafer, and Y. T. Lee, *J. Chem. Phys.* **82,** 3067 (1985).

25 M. Faubel, L. Rusin, S. Schlemmer, F. Sondermann, U. Tappe, and J. P. Toennies, *J. chem. Soc., Faraday Trans.* **89,** 1475 (1993).

26 M. Faubel, L. Y. Rusin, S. Schlemmer, F. Sondermann, U. Tappe, and J. P. Toennies, *J. Chem. Phys.* **101,** 2106 (1994).

27 Faubel, *Z. Phys. Chem.* **188,** 197 (1995).

28 G. Dharmasena, T. R. Phillips, K. N. Shokirev, G. A. Parker, and M. Keil, *J. Chem. Phys.* **106,** 9950 (1997).

29 W. B. Chapman, B. W. Blackmon, and D. J. Nesbitt, (in preparation).

30 D. Proch and T. Trickl, *Rev. Sci. Instrum.* **60,** 713 (1989).

31 D. Herriott, H. Kogelnik, and R. Kompfner, *Appl. Opt.* **3,** 523 (1964).

32 J. L. Hall and S. A. Lee, *Appl. Phys. Lett.* **29,** 367 (1976).

33 W. B. Chapman, M. J. Weida, and D. J. Nesbitt, *J. Chem. Phys.* **106,** 2248 (1997).

34 E. Arunan, D. W. Setser, and J. F. Ogilvie, *J. Chem. Phys.* **97,** 1734 (1992).

BIBLIOGRAPHY

J. G. Anderson and F. Kaufman, *Chem. Phys. Lett.* **19,** 483 (1973).

F. J. Aoiz, L. Banares, V. J. Herrero, V. Saez Rabanos, K. Stark, and H.-J. Werner, *J. Chem. Phys.* **102,** 10665 (1994).

E. Arunan, D. W. Setser, and J. F. Ogilvie, *J. Chem. Phys.* **97,** 1734 (1992).

F. E. Bartoszek, D. M. Manos, and J. C. Polanyi, *J. Chem. Phys.* **69,** 933 (1978).

C. F. Bender, P. K. Pearson, S. V. ONeil, and H. F. Schaefer III, *J. Chem. Phys.* **56,** 4626 (1972).

S. E. Bradforth, D. W. Arnold, D. M. Neumark, and D. E. Manolopouls, *J. Chem. Phys.* **99,** 6345 (1993).

G. Brasseur and S. Solomon, *Aeronomy of the Middle Atmosphere* (Reidel, Dordrecht, 1986).

J. Brion, A. Chakir, D. Daumont, J. Malicet, and C. Parisse, *Chem. Phys. Lett.* **213,** 610 (1993).

J. E. Butler, L. D. Talley, G. K. Smith, and M. C. Lin, *J. Chem. Phys.* **74,** 4501 (1981).

J. F. Castillo, D. E. Manolopoulous, K. Stark, and H.-J. Werner, *J. Chem. Phys.* **104,** 6531 (1996).

S. A. Chapman, *Mem. Roy. Meterol. Soc.* **3,** 103 (1930).

W. B. Chapman, , University of Colorado, Boulder, 1997.

W. B. Chapman, M. J. Weida, and D. J. Nesbitt, *J. Chem. Phys.* **106,** 2248 (1997).

W. B. Chapman, B. W. Blackmon, and D. J. Nesbitt, (in preparation).

P. E. Charters, R. G. Macdonald, and J. C. Polanyi, *Appl. Opt.* **10,** 1747 (1971).

E. Coleman, T. Siegrist, D. A. Mixon, P. L. Trevor, and D. J. Trevor, *J. Vac. Sci. Technol.* **A9,** 2408 (1991).

R. N. Coltharp, S. D. Worley, and A. E. Potter, *Appl. Opt.* **10,** 1786 (1971).

G. A. Cook, A. D. Kiffer, C. V. Klumpp, A. H. Malik, and L. A. Spence, *Ozone Chemistry and Technology* (American Chemical Society, Washington, 1959).

J. A. Coxon, A. D. Sapey, and R. A. Copeland, *J. Mol. Spec.* **145,** 41 (1991).

D. Daumont, J. Brion, J. Charbonnier, and J. Malicet, *J. Atmos. Chem.* **15,** 145 (1992).

J. E. Davenport, B. Ridley, H. I. Schiff, and K. H. Welge, *J. Chem. Soc. Faraday Disc.* **53,** 230 (1972).

J. A. Davidson, H. I. Schiff, T. J. Brown, and C. J. Howard, *J. Chem. Phys.* **69,** 4277 (1978).

W. B. DeMore, S. P. Sander, D. M. Golden, R. F. Hampson, M. J. Kurylo, C. J. Howard, A. R. Ravishankara, C. E. Kolb, and M. J. Molina, (Jet Propulsion Laboratory, Pasedena, 1994).

G. Dharmasena, T. R. Phillips, K. N. Shokirev, G. A. Parker, and M. Keil, *J. Chem. Phys.* **106,** 9950 (1997).

G. H. Dieke and H. M. Crosswhite, *J. Quant. Spectrosc. Radiat. Transfer* **2,** 97 (1962).

J. A. Dodd, S. J. Lipson, and W. A. M. Blumberg, *J. Chem. Phys.* **95,** 5752 (1991).

Scientific Assessment of Ozone Depletion: 1994, Vol. , edited by C. A. Ennis (World Meterological Organization, 1995).

M. Faubel, L. Rusin, S. Schlemmer, F. Sondermann, U. Tappe, and J. P. Toennies, *J. chem. Soc., Faraday Trans.* **89,** 1475 (1993).

M. Faubel, L. Y. Rusin, S. Schlemmer, F. Sondermann, U. Tappe, and J. P. Toennies, *J. Chem. Phys.* **101,** 2106 (1994).

Faubel, *Z. Phys. Chem.* **188,** 197 (1995).

B. J. Finlayson-Pitts and T. E. Kleindienst, *J. Chem. Phys.* **74,** 5643 (1981).

G. P. Glass, H. Endo, and B. K. Chaturvedi, *J. Chem. Phys.* **77,** 5450 (1982).

J. L. Hall and S. A. Lee, *Appl. Phys. Lett.* **29,** 367 (1976).

W. N. Hartley, *J. Chem. Soc.* **39,** 111 (1881).

A. G. Hearn, *Proc. Phys. Soc. London* **78,** 932 (1961).

D. Herriott, H. Kogelnik, and R. Kompfner, *Appl. Opt.* **3,** 523 (1964).

R. L. Jaffe, J. M. Henry, and J. B. Anderson, *J. Chem. Phys.* **59,** 1128 (1973).

W. Jakubetz and J. N. L. Connor, *Faraday Discuss. Chem. Soc.* **62,** 324 (1977).

M. J. Kurylo, *Chem. Phys. Lett.* **23,** 467 (1973).

J. M. Launay and M. Le Dourneuf, *Chem. Phys. Lett.* **169,** 473 (1990).

L. C. Lee and T. G. Slanger, *J. Chem. Phys.* **69,** 4053 (1978).

J. H. Lee, J. V. Michael, W. A. Payne, and L. J. Stief, *J. Chem. Phys.* **69,** 350 (1978).

G. C. Light and J. H. Matsumoto, *Chem. Phys. Lett.* **58,** 578 (1978).

G. C. Lynch, R. Steckler, D. W. Schwenke, A. J. C. Varandas, and D. G. Truhlar, *J. Chem. Phys.* **94,** 7136 (1991).

D. E. Manolopoulos, K. Stark, H.-J. Werner, D. W. Arnold, S. E. Bradforth, and D. M. Neumark, *Science* **262** (1993).

D. E. Manolopoulos, *J. Chem. soc., Faraday Trans.* **93,** 673 (1997).

E. R. Manzanares, M. Suto, and L. C. Lee, *J. Chem. Phys.* **85,** 5027 (1986).

K. J. Mauersberger, D. Hanson, and J. Morton, *Geophys. Res. Lett.* **13,** 671 (1986).

D. H. Maylotte, J. C. Polanyi, and K. B. Woodall, *J. Chem. Phys.* **57,** 1547 (1972).

G. Mount, *J. Geophys. Res.* **97,** 2427 (1992).

J. T. Muckerman, *J. Chem. Phys.* **57,** 3382 (1972).

D. D. Nelson Jr, A. Schiffman, and D. J. Nesbitt, *J. Chem. Phys.* **93,** 7003 (1990).

D. Neuhauser, R. S. Judson, R. L. Jaffe, M. Baer, and D. J. Kouri, *Chem. Phys. Lett.* **176,** 546 (1991).

D. M. Neumark, A. M. Wodtke, G. N. Robinson, C. C. Hayden, and Y. T. Lee, *J. Chem. Phys.* **82,** 3045 (1985).

D. M. Neumark, A. M. Wodtke, G. N. Robinson, C. C. Hayden, K. Shobatake, R. K. Sparks, T. P. Schafer, and Y. T. Lee, *J. Chem. Phys.* **82,** 3067 (1985).

H. Ohoyama, T. Kasai, Y. Yoshimura, H. Kimura, and K. Kuwata, *Chem. Phys. Lett.* **118,** 263 (1985).

J. C. Polanyi and K. B. Woodall, *J. Chem. Phys.* **57,** 1574 (1972).

A. E. Potter, R. N. Coltharp, and S. D. Worley, *J. Chem. Phys.* **54,** 992 (1970).

D. Proch and T. Trickl, *Review of Scientific Instruments* **60,** 713 (1989).

A. R. Ravishankara, P. H. Wine, and A. O. Langford, *J. Chem. Phys.* **15,** 984 (1979).

K. N. Rensberger, J. B. Jeffries, and D. R. Crosley, *J. Chem. Phys.* **90,** 2174 (1988).

T. P. Schafer, P. E. Siska, J. M. Parson, F. P. Tully, Y. C. Wong, and Y. T. Lee, *J. Chem. Phys.* **53,** 3385 (1970).

A. Schiffman, D. D. Nelson Jr., M. S. Robinson, and D. J. Nesbitt, *J. Phys. Chem.* **95,** 2629 (1991).

A. Schiffman and D. J. Nesbitt, *J. Chem. Phys.* **95,** 2629 (1991).

A. Schiffman and D. J. Nesbitt, *J. Chem. Phys.* **100,** 2677 (1994).

A. Sinha, E. R. Lovejoy, and C. J. Howard, *J. Chem. Phys.* **87,** 2122 (1987).

C. A. Smith, L. T. Molina, J. J. Lamb, and M. J. Molina, *Int. J. Chem. Kin.* **16,** 42 (1984).

I. Smith and M. D. Williams, *Farad. Trans. 2* **81,** 1849 (1985).

J. E. Spencer, H. Endo, and G. P. Glass, *16th (International) Sympolium on Combustion* **,** 829 (1976).

K. Stark and H.-J. Werner, *J. Chem. Phys.* **104,** 6515 (1996).

R. Steckler, D. G. Truhlar, and B. C. Garrett, *J. Chem. Phys.* **82,** 5499 (1985).

G. E. Streit, C. J. Howard, A. L. Schmeltekopf, J. A. Davidson, and H. I. Schiff, *J. Chem. Phys.* **65,** 4761 (1976).

G. E. Streit and H. S. Johnston, *J. Chem. Phys.* **64,** 95 (1976).

R. A. Sutherland and R. A. Anderson, *J. Chem. Phys.* **58,** 1226 (1973).

T. Takayanagi and S. Sato, *Chem. Phys. Lett.* **144,** 191 (1988).

R. P. Wayne, *Chemistry of Atmospheres* (Clarendon Press, Oxford, 1991).

P. H. Wine and A. R. Ravishankara, *Chem. Phys.* **69,** 365 (1982).

M. S. Zahniser and C. J. Howard, *J. Chem. Phys.* **73,** 1620 (1980).

J. Z. H. Zhang, *Chem. Phys. Lett.* **181,** 63 (1991).

J. Z. H. Zhang and W. H. Miller, *J. Chem. Phys.* **88,** 4549 (1991).

APPENDIX A

PROGRAMMING THE DSP TRANSIENT DIGITIZER/AVERAGING MEMORY

The DSP Technology, Inc. MODEL 2001AS is a 100MHz, 8-bit analog to digital converter. Connected to the 2001AS is the MODEL 4101 averaging memory. These units are powered by a CAMAC crate and are controlled through the CC-488 GPIB crate controller. The 2001AS and 4101 can only be controlled through the CC-488 via computer. Hence, successful operation of the DSP modules requires an in-depth understanding of the various CAMAC and GPIB codes.

When working with the DSP system, be aware: *THERE ARE MISTAKES IN THE MANUALS!* These various mistakes have impeded my progress many times, and whenever possible, I have noted the mistake. However, I have not used every aspect of the DSP system, so I cannot attest to the truth of every aspect of every manual. One very important error is the 2001AS – 4101 connector pinout. The correct pinout is located in table A-1.

2001AS Pin #	4101 Pin #	Function	Description
9	17	TRIG	Generator: 4101. Signals the 2001AS to begin digitizing.
10	19	EOC	Generator: 2001AS. Digitizing is complete and summation can begin. Remains high until RST is generated by the 4101. (20 ns pulse width)
22	18	MEMINC (or CNTADD)	Generator: 4101. Advances the memory of the 2001AS to the next location. (80 ns pulse width)
23	20	RST (or EOR)	Generator: 4101. Sweep is complete and 2001AS can gather more data. (80 ns pulse width)
17	8	BIT 7	Most significant bit from 2001AS.
4	7	BIT 6	--
16	6	BIT 5	--
3	5	BIT 4	--
15	4	BIT 3	--
2	3	BIT 2	--
14	2	BIT 1	--
1	1	BIT 0	Least significant bit from 2001AS.
25	--	CLK (1 MHz)	1 MHz clock from 2001AS
24	--	GND	2001AS ground

Table A-1. Pin assignments for the 2001AS – 4101 interface.

Controlling the DSP system requires a fairly good understanding of the GPIB interface. The particular GPIB card in use at the time of this writing is made by National Instruments. It is packaged with libraries for virtually every language and is very well documented. The code segments contained in this chapter are written in Microsoft Visual Basic v. 5.0. The computer used is a Pentium-75 running Windows 95. The DSP system is completely unaware of the specifics of the computer attached to the other end, so most of the information contained here will be applicable to any user of the DSP.

All communication between the computer and the various DSP components are done via the crate controller, in this case the CC-488 which can transfer 321 KBytes of data per second, as shown in figure A-1. In order to communicate to any of the units in the crate, you must send the appropriate codes to the crate controller. The crate controller then relays those codes to the appropriate device. The codes specific to a particular device are given in the respective instruction manual, but all the codes have a common form.

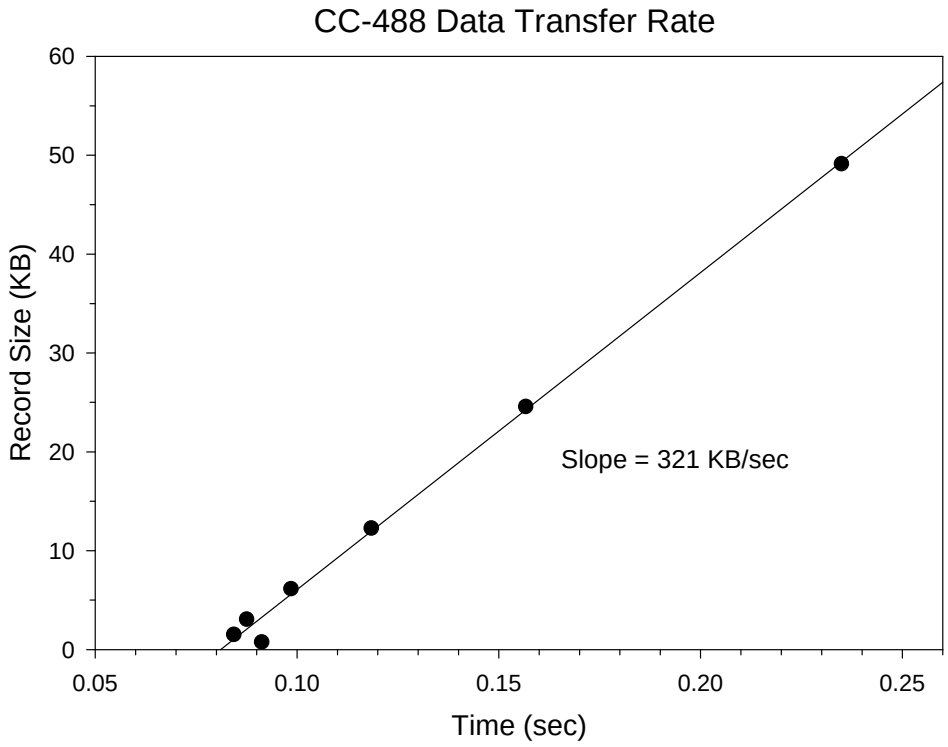

Figure A-1. The data transfer rate for the CC-488 CAMAC GPIB contoller. The slope of the above line is 321 kBytes/sec.

A.1 Reading Parameters from the DSP

Actions performed on a DSP component fall into two categories: reading and writing. In order to read a parameter on a component requires three

components: (1) an ‘N’ code, (2) an ‘A’ code, and (3) an ‘F’ code. The ‘N’ code merely refers to the position of the particular component in the crate. For example, the 4101 averaging memory is in slot 24, so a read command sent to the 4101 must begin with 24. The ‘F’ code and ‘A’ code together refer to a specific function of the component. Tables of ‘F’ codes and ‘A’ codes are given in the manual. For example, to read the module ID for the 4101, you would need to enter A(0)F(3), or 0 in the ‘A’ code place and 3 in the ‘F’ code place. Once these codes are sent to the crate controller, the controller relays these codes to the proper module. The module then returns the requested value, which the controller intercepts and relays to the computer.

Communication between the DSP and the computer is done via 8-bit binary codes. These 8-bit binary codes are most commonly thought of as the ASCII character set, as shown in table A-2.

0	·	32	[space]	64	@	96	`	128	·	160	[space]	192	À	224	à
1	·	33	!	65	A	97	a	129	·	161	¡	193	Á	225	á
2	·	34	"	66	B	98	b	130	·	162	¢	194	Â	226	â
3	·	35	#	67	C	99	c	131	·	163	£	195	Ã	227	ã
4	·	36	$	68	D	100	d	132	·	164	¤	196	Ä	228	ä
5	·	37	%	69	E	101	e	133	·	165	¥	197	Å	229	å
6	·	38	&	70	F	102	f	134	·	166	¦	198	Æ	230	æ
7	·	39	'	71	G	103	g	135	·	167	§	199	Ç	231	ç
8	* *	40	(	72	H	104	h	136	·	168	¨	200	È	232	è
9	* *	41	)	73	I	105	i	137	·	169	©	201	É	233	é
10	* *	42	*	74	J	106	j	138	·	170	ª	202	Ê	234	ê
11	·	43	+	75	K	107	k	139	·	171	«	203	Ë	235	ë
12	·	44	,	76	L	108	l	140	·	172	¬	204	Ì	236	ì
13	* *	45	-	77	M	109	m	141	·	173	-	205	Í	237	í
14	·	46	.	78	N	110	n	142	·	174	®	206	Î	238	î
15	·	47	/	79	O	111	o	143	·	175	¯	207	Ï	239	ï
16	·	48	0	80	P	112	p	144	·	176	°	208	Ð	240	ð
17	·	49	1	81	Q	113	q	145	‘	177	±	209	Ñ	241	ñ
18	·	50	2	82	R	114	r	146	’	178	²	210	Ò	242	ò
19	·	51	3	83	S	115	s	147	·	179	³	211	Ó	243	ó
20	·	52	4	84	T	116	t	148	·	180	´	212	Ô	244	ô
21	·	53	5	85	U	117	u	149	·	181	µ	213	Õ	245	õ
22	·	54	6	86	V	118	v	150	·	182	¶	214	Ö	246	ö
23	·	55	7	87	W	119	w	151	·	183	·	215	×	247	÷
24	·	56	8	88	X	120	x	152	·	184	¸	216	Ø	248	ø
25	·	57	9	89	Y	121	y	153	·	185	¹	217	Ù	249	ù
26	·	58	:	90	Z	122	z	154	·	186	º	218	Ú	250	ú
27	·	59	;	91	[	123	{	155	·	187	»	219	Û	251	û
28	·	60	<	92	\	124	|	156	·	188	¼	220	Ü	252	ü
29	·	61	=	93	]	125	}	157	·	189	½	221	Ý	253	ý
30	·	62	>	94	^	126	~	158	·	190	¾	222	Þ	254	þ
31	·	63	?	95	_	127	·	159	·	191	¿	223	ß	255	ÿ

Table A-2. The ASCII character set. The characters denoted by (·) do not have a visual representation. Asterisks (**) represent control characters, such as the carriage return (ASCII code 13).

Therefore, when the ‘N’ code “24” is sent, one doesn’t send the digits 2 and 4, but the ASCII equivalent of 24 which doesn’t have a visual representation (binary 00011000). The controller expects three eight bit streams in succession. These streams are identified by the order received, which is the ‘N’ code, ‘A’ code and ‘F’ code, respectively. The return value is a stream of one to three bytes, which must be reassembled into the correct integer return code. The following piece of code queries the module ID of the 4101 averaging memory which is located in slot 24:

```
Model_Number = CrateRead(24,0,3)    ‘Calls CrateRead Function
Print Model_Number                  ‘Prints 4101

Private Function CrateRead(NCode As Long, ACode As Long,
                           FCode As Long) As Long
Dim NumResult(3) As Integer
Dim i As Integer

NCode$ = Chr(Ncode)
ACode$ = Chr(Acode)
FCode$ = Chr(Fcode)

ReturnBuffer$ = Space(3) ‘Allocate Space
WriteString$ = Space(3)  ‘for Buffers

WriteString$ = NCode$ & ACode$ & FCode$ 'Concatenate all the
strings

Call ibwrt(DSPLocation%, WriteBuffer$)      ‘Send string to DSP
Call ibrd(DSPLocation%, ReturnBuffer$)    ‘Retrive string from DSP


For i = 1 To 3          'Convert the string from DSP to integers
    NumResult(i) = Asc(Mid(ReturnBuffer$, i, 1))
Next i

CrateRead = 0
For i = 1 To 3
    CrateRead = CrateRead + NumResult(i) * 2 ^ ((i - 1) * 8)
Next i                      ‘Put the integers together
                            ‘to form one integer

End Function
```

The `ibwrt()` and `ibrd()` functions are functions defined by the driver software for the particular GPIB card currently used in the lab. The functions take a string of ASCII characters and send them as their binary equivalents over the GPIB line. Obviously the number '4101' cannot be expressed by the DSP system as a single 8 bit number, so the crate controller breaks up the number into three 8 bit streams and sends them in the order of least significant byte to most significant byte. In order to read the result in a convenient way, the bytes must be reassembled to form the expected integer. If we were to examine each of the bytes from the DSP, we would see the following: 00000101 00010000 000 00000, which are the numbers 5, 16, and 0, respectively. Noting that the smallest byte is first, the result is given by:

result = $5 + (16*2^8) + (0 * 2^{16}) = 4096 + 5 = 4101$,

which is the model number for the averaging memory.

A.2 Writing Parameters to the DSP

Writing a parameter to a DSP component is very similar to reading parameters. The write codes contain the familiar 'N', 'A', and 'F' codes, with the addition of another three-byte word known as the 'W' code. Again, all these codes must be converted to their ASCII-character equivalent before being sent. The following example demonstrates changing the number of averages on the 4101. The 4101 is programmed to stop summing when the number of sweeps reaches 65536. In order to obtain a number of averages less than 65536, you must set the initial value of the sweep register to 65536-n, where n is the desired number of averages, or sweeps. For the purposes of this example, the number of desired averages will be 5.

```
AverageNumber = 5
WCode = 65536-AverageNumber
Result = CrateWrite(24,0,17,Wcode)

If Result = 0 then
      Print “Success!”
Else
      Print “Failure!”
End if

Private Function CrateWrite(Ncode as long, Acode as long,
            Fcode as long, Wcode as long) As Integer

Dim Wdata3 As Integer
Dim Wdata2 As Integer
Dim Wdata1 As Integer

On Error GoTo Errorhandler

WriteString$ = Space(3)
WriteString2$ = Space(3)

'Breaks the WCode into three bytes----------------------
Wdata3 = Int(WCode / 2 ^ 16)
Wdata2 = Int(WCode / 2 ^ 8) - Wdata3 * 2 ^ 8
Wdata1 = Int(WCode) - Wdata3 * 2 ^ 16 - Wdata2 * 2 ^ 8
'-------------------------------------------------------

NCode$ = Chr(NCode)         ‘Create Function Code to
ACode$ = Chr(ACode)         ‘send to DSP
FCode$ = Chr(FCode)

WriteString$ = Space(3)             ‘Allocate space for buffers
WriteString2$ = Space(3)

WriteString$ = NCode$ & ACode$ & FCode$         ‘Concatenate the
                                                ‘strings
WriteString2$ = Chr(Wdata1) & Chr(Wdata2) & Chr(Wdata3)

Call ibwrt(DSPLocation%, WriteString$)      'Send the function
codes
Call ibwrt(DSPLocation%, WriteString2$)     'Send the Write code

CrateWrite = 0
Exit Function

Errorhandler:
CrateWrite = -1

End Function
```

It is important to note the size of the integers being written to the DSP. In this case, the integer size is 65531, which is a number too large for the integer data type to hold. Therefore, it is necessary to work with 4-byte integers or the long data

type (see table A-3). In addition, it is again important to break up the long integer into a 3-byte word in the order of least significant byte to most significant byte.

Data Type	Size	Range
Byte	1 byte	0 to 255
Boolean	2 bytes	True or False
Integer	2 bytes	-32,768 to 32,767
Long (long integer)	4 bytes	-2,147,483,648 to 2,147,483,647
Single (single-precision floating-point)	4 bytes	-3.402823E38 to -1.401298E-45 for negative values; 1.401298E-45 to 3.402823E38 for positive values
Double (double-precision floating-point)	8 bytes	-1.79769313486232E308 to -4.94065645841247E-324 for negative values; 4.94065645841247E-324 to 1.79769313486232E308 for positive values
Currency (scaled integer)	8 bytes	-922,337,203,685,477.5808 to 922,337,203,685,477.5807
Decimal	14 bytes	+/-79,228,162,514,264,337,593,543,950,335 with no decimal point; +/-7.9228162514264337593543950335 with 28 places to the right of the decimal; smallest non-zero number is +/-0.0000000000000000000000000001
Date	8 bytes	January 1, 100 to December 31, 9999
Object	4 bytes	Any Object reference
String (variable-length)	10 bytes + string length	0 to approximately 2 billion

Table A-3. Data Types and sizes.

A.3 Block Transfer

There is a special mode for the transfer of entire traces. The block transfer mode is very similar to the read mode, but instead of sending a single 3 byte word, the controller sends a stream of 3 byte words representing every point in the trace. These streams are intercepted by the GPIB software and stored as a string. The largest trace that can be stored by the digitizer/memory combination is 32768 data points (32K). Each point is represented by a 3 byte word which results in a string that is at most 98304 bytes long. In order to read the data, the software must loop through the string and combine every three bytes into a single long integer and store that integer in an array. Each element in that array must then be divided by the number of sweeps made by the averaging memory in order to yield the true average of the data. The following code demonstrates initiating the block transfer command to the 4101 and interpreting the results.

```
Private Sub BlockTransfer(NCode as long, FCode as long,
            ACode as long, RecLength as long, AverageNum as long)

Dim Length As Long
Dim result(1 To 3) As Long

Buffer$ = Space(3 * RecLength)      ‘Allocate enough space
WriteString$ = Space(3)             ‘for buffers

NCode$ = Chr(NCode)                 ‘create ASCII character
ACode$ = Chr(ACode)                 ‘representations
FCode$ = Chr(FCode)
WriteString$ = NCode$ & ACode$ & FCode$


Call ibwrt(DSPLocation%, WriteString$)    ‘Send the command

Call ibrd(DSPLocation%, Buffer$)          ‘Receive the data

Length = RecLength * 3
ReDim Data(RecLength)         ‘Dimension the data array
```

```
k = 0
For i = 1 To Length Step 3

    result(1) = Asc(Mid(Buffer$, i, 1))
    result(2) = Asc(Mid(Buffer$, i + 1, 1))
    result(3) = Asc(Mid(Buffer$, i + 2, 1))

‘Convert the array to integers---------------------
      Data1(k) = result(1) + (result(2) * 256) +
      (result(3) * 65536)
‘-------------------------------------------------

‘Convert the integers to Volts-----------------------
      Data1(k) = ((Data1(k) / AverageNum) – 129) / 493
 ‘-----------------------------------------------------
    k = k + 1
Next i

End Sub
```

A.4 Setting up the Digitizer/Averaging Memory

The power on state of the DSP system is not suitable for taking data. There are a few key variables that must be initialized. A system initialization flow chart is contained in figure A-2. Setting up the 2001AS digitizer requires sending a single 11-bit integer. The value of this integer determines the number of pretrigger samples, record length, and sampling interval. Table A-4 contains the correct bit positions for each parameter. It is important to make sure the record length for the 4101 and the 2001AS are set to the same value.

Parameter	Value	Bit Position										
		11	10	9	8	7	6	5	4	3	2	1
Pre-Trig Samples	0	--	--	--	--	--	--	--	--	0	0	0
	1/8	--	--	--	--	--	--	--	--	0	0	1
	2/8	--	--	--	--	--	--	--	--	0	1	0
	3/8	--	--	--	--	--	--	--	--	0	1	1
	4/8	--	--	--	--	--	--	--	--	1	0	0
	5/8	--	--	--	--	--	--	--	--	1	0	1
	6/8	--	--	--	--	--	--	--	--	1	1	0
	7/8	--	--	--	--	--	--	--	--	1	1	1
Record Length	256	--	--	--	--	--	1	0	1	--	--	--
	512	--	--	--	--	--	1	0	0	--	--	--
	1024	--	--	--	--	--	0	1	1	--	--	--
	2048	--	--	--	--	--	0	1	0	--	--	--
	4096	--	--	--	--	--	0	0	1	--	--	--
	8192	--	--	--	--	--	0	0	0	--	--	--
	16384	--	--	--	--	--	1	1	0	--	--	--
	32768	--	--	--	--	--	1	1	1	--	--	--
Sampling Interval	10ns	--	--	0	0	0	--	--	--	--	--	--
	20ns	--	--	0	0	1	--	--	--	--	--	--
	50ns	--	--	0	1	0	--	--	--	--	--	--
	100ns	--	--	0	1	1	--	--	--	--	--	--
	200ns	--	--	1	0	0	--	--	--	--	--	--
	500ns	--	--	1	0	1	--	--	--	--	--	--
	1000ns	--	--	1	1	0	--	--	--	--	--	--
	Ext. Clk.	--	--	1	1	1	--	--	--	--	--	--
Local		1	--	--	--	--	--	--	--	--	--	--
Remote		0	--	--	--	--	--	--	--	--	--	--

Table A-4. Bit positions for the setup parameters for the 2001AS.

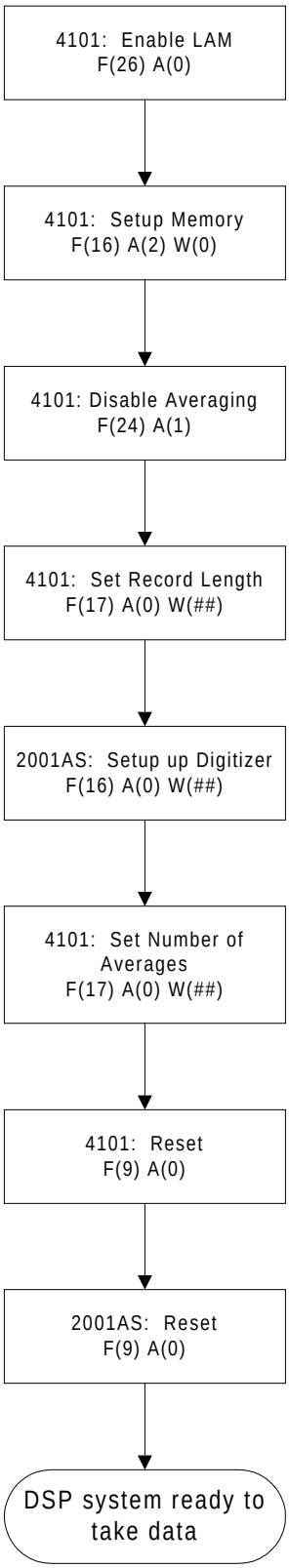

Figure A-2. Flow chart outlining the procedure for initializing the 4101/2001AS

A.5 Using the Digitizer/Averaging Memory

Using the 2001AS/4101 combination is fairly straight forward, but there are a few caveats. First of all, the signal input for the 2001AS has a 50 ohm input impedance. Also, the input dynamic range for the 2001AS is 0.5 volts. There is included on the 2001AS a trimpot labeled "Offset Adjust" which allows the user to move the 0.5 volt input range about 0.0 volts. Currently, the offset adjust is set to 0.25 volts, which allows the 2001AS to accept voltages between –0.25 volts and 0.25 volts. Any voltages outside the range of the 2001AS are clipped.

The 2001AS is an 8-bit digitizer which means the input voltage can take any integer value between 0 and 255. Converting these values back into voltage requires knowledge of two parameters: the offset and the voltage step size. The offset is easily changed on the front panel of the 2001AS, but the step size is built into the analog to digital circuitry of the 2001AS. Currently, the offset adjust is set to 0.25 volts or a digital value of 129. This implies that a grounded input will output a digital value of 129; a value of –0.25 volts will yield a digital value of 0; and a value of 0.25 volts will yield a digital value of 255. A plot of voltage vs digital value for a number of points is contained in figure A-3. The numbers from this plot have been included in the software to convert the digital value to a voltage value using the following equation:

$$\text{Voltage} = \frac{\text{digital\_number} - 129}{493\ \text{volts}^{-1}}.$$

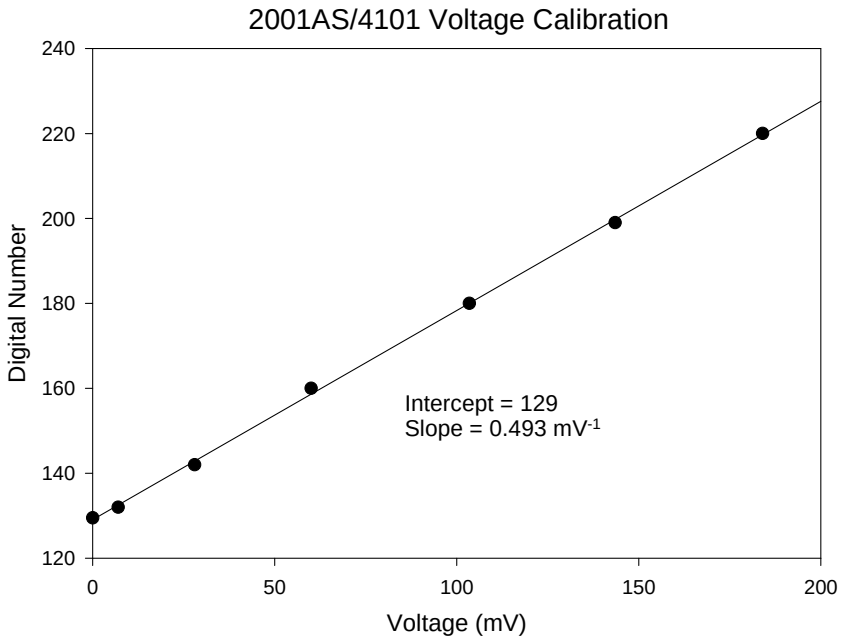

Figure A-3. Voltage calibration plot for the 4101. The above line has an intercept of 129 and a slope of 493 volts^{-1}.

Be aware that the 4101 does not divide the values in its memory by the number of sweeps. In that respect, it is not a rigorous averager , but instead only a summer. It is up to the user to divide the result by the number of sweeps acquired.

A.6 The Scanner 1.0 Program

Scanner 1.0 is the first program written to take advantage of the abilities of the 2001AS/4101 combination. A line by line explanation of the code is beyond the scope of this thesis, but a brief overview of the algorithms and equations involved is appropriate. The program is designed to be a graphical, user-friendly gated integrator and frequency controller to the F-Center laser in B214. The software uses the DSP system for the acquisition of the transient absorbance signals and uses an

inexpensive National Instruments A-D/D-A card for the acquisition of various other DC voltages and laser frequency control. The software displays the absorbance signal, the TAC signal from a scanning fabry-perot etalon, and the IR DC power . The program uses a gated integration technique for gathering data at each frequency. The user is able to choose the position and width of two gates, one that includes baseline and the other that includes the transient absorbance signal. The software sums the points in each gate and calculates the difference. That difference can be compared to the IR DC level to yield an absorbance value. A flow chart containing the algorithm for the primary data taking loop is contained in figure A-4.

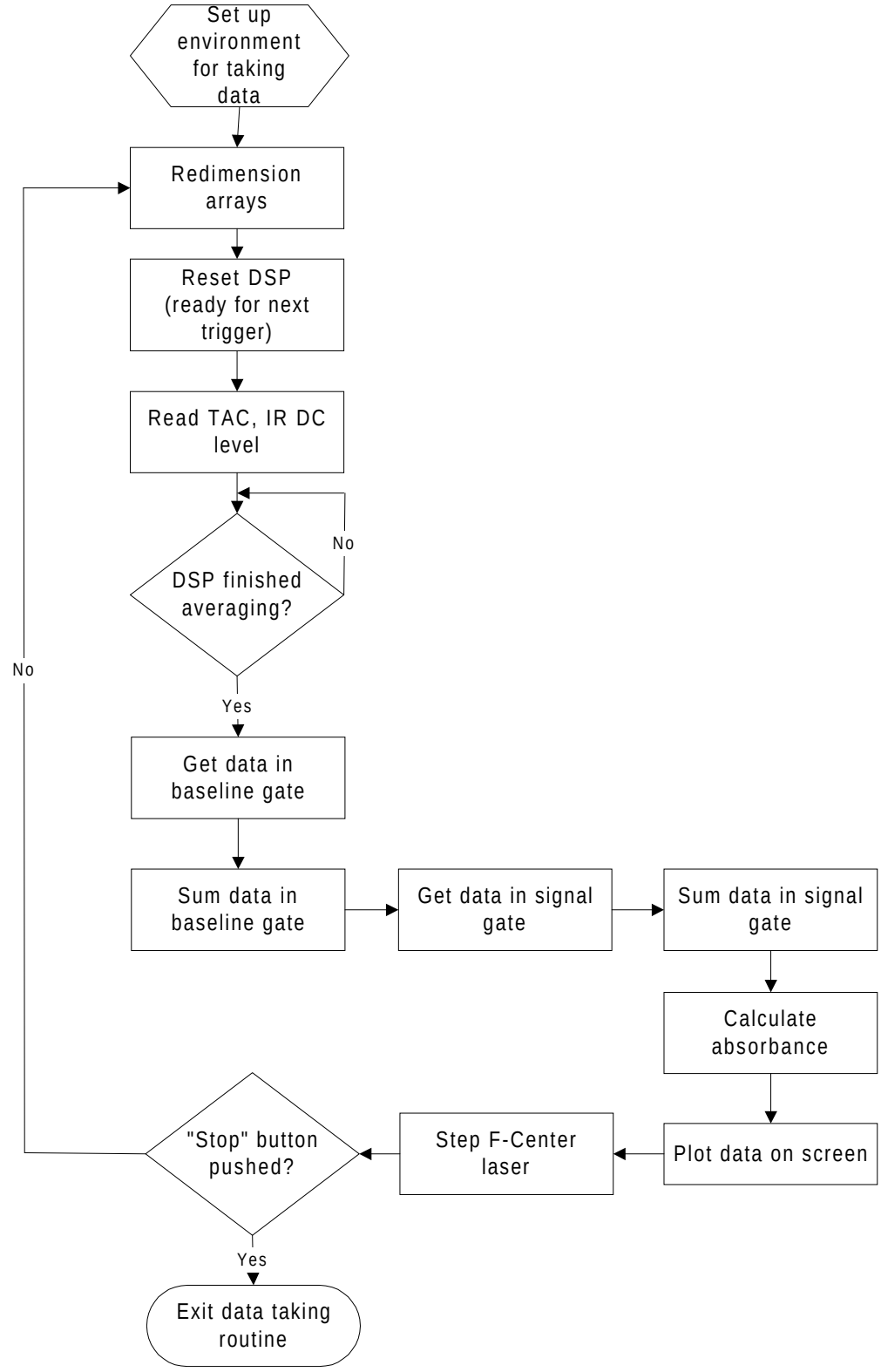

Figure A-4. Flow chart outlining the data taking subroutine in Scanner 1.0.

There are a few notable features about the loop contained in figure A-4. First of all, only the data within the gates is transferred from the DSP. This reduces the amount of data transferred and increases the speed at which data can be taken. Secondly, the equation for calculating the absorbance is as follows:

$$A = -\ln\left(-\frac{\text{SignalSum} - \text{BaseSum}}{\text{GateWidth} \times \text{Gain} \times \text{DCLevel}} + 1\right),$$

where Gain is the total gain of the subtracted signal and DCLevel is the amount of IR light (in volts) on the reference detector. This equation is valid as long as the signal gate and the baseline gate are of the same size, which is a requirement in this particular version of Scanner.

Scanner 1.0 saves the data and parameters to a binary file. This saves disk space and file access time. However, working with binary files requires forehand knowledge of the order and type of variables in the file. The following is a section of the subroutine that saves the binary file.

```
Open FileName For Binary As #3
Put #3, , Index               'Number of data points (integer)
Put #3, , PreTrig             'DSP pre-trigger samples (integer)
Put #3, , SampInterval        'DSP sampling interval (integer)
Put #3, , RecLength           'DSP record length (long integer)

Put #3, , Data                'Data structure that holds all data
Close #3
```

The data structure `Data` has the following format:

```
Type DataRecord
    SignalData() As Single    'Subtracted signal (Volts)
    Absorbance() As Single    'Calculated Absorbance
    IRData() As Single        'IR DC level (Volts)
    TACdata() As Single       'TAC data (Volts)
    Average As Integer        'Number of averages
    Index As Long             'Number of data points
    FrequencyStep As Integer  'F-Center Step size
    Gain() As Single          'Reported Gain at each point
    SigGate1 As Long          'Index of start of signal gate
```

```
    SigGate2 As Long          'Index of end of signal gate
    BaseGate1 As Long         'Index of start of baseline gate
    basegate2 As Long         'Index of end of baseline gate
    GateWidth As Long         'Width of signal and baseline gate
    XScale As Long            'Scanner 1.0 horizontal zoom factor
    Frequency() As Single     'Frequency of each point
    FrequencyIndex As Long    'Number of frequency markers in scan
    FrequencyMarker() As Long 'Location of frequency markers
End Type
```

The sizes of each data type are given in table A-3.

In order to read the binary file into another program, the programmer must make a compatible data structure to the one shown above. The actual data names are irrelevant, but the sizes of each variable and array are crucial. Next, one must open the proper file and read the first four integers (the last of which is a long integer). Now, the file can be read into the compatible structure. The following is an example of a routine that correctly reads a Scanner 1.0 file:

```
'Scanner 1.0 Type Definition--------------------
Type Scanner1Data
    SignalData() As Single
    Absorbance() As Single
    IRData() As Single
    TACdata() As Single
    Average As Integer
    Index As Long
    FrequencyStep As Integer
    Gain() As Single
    SigGate1 As Long
    SigGate2 As Long
    BaseGate1 As Long
    BaseGate2 As Long
    GateWidth As Long
    XScale As Long
    Frequency() As Single
    FrequencyIndex As Long
    FrequencyMarker() As Long
End Type
'-------------------------------------------------


'Dimension Some Local Variables----
Dim Scn1 As Scanner1Data
```

```
Dim PreTrig As Integer
Dim SampInterval As Integer
Dim RecLength As Long
'---------------------------------

'Open file for read-only,binary acces------
Open FileName For Binary Access Read As #1
'-----------------------------------------

'Get some initial data parameters---------
Get #1, , Index
Get #1, , PreTrig
Get #1, , SampInterval
Get #1, , RecLength
'---------------------------------------

'Get Majority of data---------------------
Get #1, , Scn1
'---------------------------------------

'Close File---------
Close #1
'-------------------
```